UNIVERSIDADE DE LISBOA

FACULDADE DE CIÊNCIAS

DEPARTAMENTO DE ENGENHARIA GEOGRÁFICA, GEOFÍSICA E ENERGIA

# Wave climate in a global warming scenario: simulations with a CMIP5 ensemble

Gil Lemos

**Mestrado em Ciências Geofísicas**
Meteorologia

Dissertação orientada por:

Prof. Dr. Álvaro Semedo
Prof. Dr. Pedro Miranda

2016

# Resumo

As ondas gravíticas geradas pelo vento na superfície do oceano são as mais energéticas do espectro, sendo responsáveis por mais de metade da energia presente em todas as ondas nesta superfície (Kinsman, 1965). São geradas pela transferência de momento do vento para a água e dominam o espectro de ondas oceânicas, ultrapassando a contribuição das marés, das "storm surges", dos tsunamis, etc. (Munk, 1951). Pela sua prevalência no oceano e influência nas actividades humanas, o seu estudo deve ser aprofundado, e as potenciais alterações no seu regime devem ser tidas em conta. Porém, apesar da sua relevância, não existe ainda nenhum modelo teórico preciso de geração e crescimento das ondas, dado que os mecanismos presentes nestes fenómenos não são ainda totalmente compreendidos por forma a serem correctamente quantificados.

Quando o vento sopra sobre a superfície do oceano, ondas são formadas pela transferência de momento no sentido da água. Esta perturbação inicial pode desenvolver-se se o vento continuar a soprar de forma constante, sendo que as ondas irão crescer até atingirem o seu nível de saturação. Os dois principais tipos de ondas à superfície do oceano são denominados "wind sea" ou apenas "sea", e "swell". As ondas de "sea" detêm alta frequência e curtos comprimentos de onda, estando directamente associadas ao campo de vento sobrejacente, crescendo rapidamente e depressa atingindo o nível de saturação. Por sua vez, as ondas de "swell", com frequências mais baixas e comprimentos de onda maiores, crescem lentamente e podem propagar-se com velocidades de fase superiores à velocidade do vento, uma vez que também extraem energia de ondas com mais alta frequência, devido a interações não lineares entre as ondas. Estas ondas podem propagar-se por milhares de quilómetros (Barber and Ursell, 1948; Munk *et al.*, 1963; Snodgrass *et al.*, 1966) com muito ligeira atenuação (Ardhuin *et al.*, 2009). Assim sendo, é possível assumir que existe uma ligação causal entre, por exemplo, um evento local de erosão costeira e uma tempestade que ocorreu "do outro lado" do mundo (em outro hemisfério). Este é apenas um dos factores interessantes que motivam a execução deste trabalho de análise das futuras alterações no clima de ondas global, uma vez que as alterações climáticas atmosféricas locais no vento podem propagar-se sob a forma de ondas à superfície do oceano, e gerar impactos a longas distâncias.

Até recentemente, o impacto das alterações climáticas no clima de ondas futuro tinha recebido muito pouca atenção. Nos últimos anos, alguns estudos foram realizados, sob os auspícios do COWCLIP (Coordinated Ocean Wave Climate Project), utilizando um único

modelo e um único cenário de concentração de gases de efeito estufa (CMIP3), recebendo atenção moderada por parte do IPCC-AR5 (Intergovernmental Panel for Climate Change - Fifth Assessment Report). No presente estudo, o impacto do aquecimento global no clima de ondas global é investigado, através de um "ensemble" composto por 2 membros (simulações do modelo de ondas WAM) de um conjunto maior, composto por 8 simulações dinâmicas e 20 simulações estatísticas, denominado GLOWAVES-2, e pertencente ao projecto COWCLIP. O (único) forçamento destas duas simulações (em termos de velocidade do vento e cobertura oceânica de gelo) provém do modelo climático EC-Earth, seguindo um cenário de elevadas emissões de gases de efeito estufa (RCP8.5). Ambas as simulações cobrem um período total de 130 anos (1971-2100), no entanto, para efeitos de análise comparativa, dois períodos mais curtos são utilizados como referência: o "clima presente" (PC20: média das duas simulações (PC20-1 e PC20-4); 1971-2000) e o "clima futuro" (projectado; FC21: média das duas simulações (FC21-1 e FC21-4); 2071-2100). O período de referência histórico (1971-2005) foi validado através da comparação com a reanálise ERA-Interim, do ECMWF (European Centre for Medium-Range Weather Forecasts) e com dados observacionais de bóias, revelando que o modelo WAM, com forçamento do EC-Earth, é capaz de produzir cenários realistas do clima de ondas global no final do século XX, fornecendo a confiança necessária na capacidade de simular uma alteração climática igualmente credível até ao final do século XXI. Os resultados (alterações futuras no clima de ondas como projectado pelas simulações) são obtidos através da comparação entre as médias de PC20 e FC21, para quatro variáveis diferentes: $H_S$ (altura significativa; m), $T_m$ (período médio da onda; s), MWD (direcção média da frente de onda; º), $P_w$ (potência das ondas; W/m, $= (\rho g^2/32\pi)\, T_m H_S^2$, como em Young, 1999). Para complementar os resultados destas variáveis, os impactos da alteração climática no campo do vento ($U_{10}$; velocidade do vento a 10 metros de altura; m/s) foram também analisados. Os resultados expõem médias a nível anual e sazonal (estações extremas de Inverno e Verão: DJF (Dezembro, Janeiro e Fevereiro) e JJA (Junho, Julho e Agosto)). Como forma de complemento, são também apresentadas as tendências lineares ao longo do período 2006-2100, para a altura significativa e para a potência (fluxo de energia) das ondas.

Devido às alterações climáticas, as projecções indicam alterações estatisticamente significativas em todas as variáveis analisadas, que poderão referir-se a aumentos ou decréscimos na sua intensidade, gradiente espacial ou mudanças na localização geográfica de determinados valores. No que toca à altura significativa, $H_S$, os aumentos nesta variável

dominam as projecções, essencialmente a nível anual, e durante o período JJA (verificando-se em 73.93% do oceano global), sendo no Oceano Antárctico ("Southern Ocean") que os maiores aumentos se verificam, estando esta situação directamente relacionada com uma intensificação projectada a nível da velocidade do vento ($U_{10}$) na mesma área. A região onde os decréscimos projectados se mostram mais prevalecentes é no Oceano Atlântico Norte, em particular durante DJF. A tendência linear de altura significativa projectada durante o período 2006-2100 estabelece-se, a nível anual, em 0.41 cm/década.

No que toca ao período médio, $T_m$, são esperados aumentos nos seus valores anuais e sazonais em praticamente todo o oceano global, excepto no Atlântico Norte e Pacífico Oeste durante DJF, e em maior extensão no verão boreal (JJA), em 87.48% da área de oceano global, em média. Tendo em conta os resultados para esta variável e para a altura significativa, uma vez que a potência das ondas ($P_w$) depende destes, é esperado que o seu comportamento não se diferencie muito dos anteriormente referidos. É efectivamente o que acontece nas projecções de $P_w$, onde se verifica um padrão de alterações muito semelhante ao da altura significativa, uma vez que as diferenças de $T_m$ apresentam valores reduzidos. Aumentos projectados de potência das ondas (que se observam em 81.43% do oceano global) alcançam os 30% no sector Índico do Oceano Antárctico (a sudoeste da Austrália), durante o inverno austral (JJA), sendo que o valor médio de incremento a nível global para esta estação se situa nos 7.18%. A tendência linear de potência das ondas projectada durante o período 2006-2100 estabelece-se, a nível anual, em 0.36 cm/década.

Relativamente à direcção média da frente de onda (MWD), as projecções indicam a prevalência de rotações anti-horárias (contra os ponteiros do relógio) nas latitudes médias e altas de ambos os hemisférios, associadas ao deslocamento latitudinal positivo das tempestades para latitudes mais elevadas (Arblaster *et al.*, 2011). Nas regiões tropicais e subtropicais, rotações positivas (no sentido dos ponteiros do relógio) são consistentes com uma maior contribuição de "swell" proveniente do Oceano Antárctico, especialmente durante o inverno austral (JJA), quando a sua "produção" é maior.

A análise de EOFs ("Empirical Orthogonal Functions") para os campos de $H_S$ e $P_w$ no Oceano Atlântico Norte, em termos de alterações entre o clima presente (PC20) e o projectado para o futuro (FC21), relevou que é esperado um ligeiro enfraquecimento dos principais centros de acção de ambos os campos (redução da variabilidade), a nível anual. A nível sazonal, comportamento similar foi detectado para a altura significativa, porém, a nível de

potência, um ligeiro fortalecimento dos seus centros de acção é esperado, com um deslocamento latitudinal positivo associado, de cerca de 2º. No entanto, deslocamentos da posição dos valores climatológicos máximos para latitudes mais elevadas não se verificam para o Atlântico Norte, apenas em algumas regiões do Oceano Antárctico.

**Palavras-chave:** Oceano, vento, ondas superficiais gravíticas, alteração, clima.

## Abstract

Ocean surface wind waves are of outmost relevance for practical and scientific reasons. On the one hand, waves have a direct impact in coastal erosion, but also in sediment transport and beach nourishment, in ship routing and ship design, as well as in coastal and offshore infrastructures, just to mention the most relevant. On the other hand waves are part of the climate system, and modulate most of the exchanges that take place at the atmosphere-ocean interface. In fact waves are the "ultimate" air-sea interaction process, clearly visible and noticeable. Up until recently, the impact of climate change in future wave climate had received very little attention. Some single model single scenario global wave climate projections, based on CMIP3 scenarios, were pursued and received some attention in the IPCC (Intergovernmental Panel for Climate Change) AR5 (Fifth Assessment Report). In the present study the impact of a warmer climate in the global ocean future wave climate is investigated through a 2-member "coherent" ensemble of wave climate projections: single-model, single-forcing, and single-scenario. The two ensemble members were produced with the wave model WAM, forced with wind speed and ice coverage from EC-Earth projections, following the representative concentration pathway with a high emissions scenario 8.5 (RCP8.5). The ensemble historic period has been set for 1971 to 2005. The projected changes in the global ocean wave climate are analyzed for the 2071-2100 period. The ensemble historical period is evaluated trough the comparison with the European Centre for medium-range weather forecasts (ECMWF) ERA-Interim reanalysis, and buoy observations.

**Keywords:** Ocean, wind, waves, climate, change.

## Acknowledgements

Lots of great things have happened in my life during the months that I spent working on this final thesis. I recall myself almost a year ago, being firstly introduced to this new working environment, with serious and purely scientific methodologies, thinking of how great it would be to finally embrace this type of work. What I didn't know at the time was how important and revolutionary this following year would be. How challenging, enjoyable and gratifying at the same time, to work in a field that I love, with some of the most kind and enlightened minds of the area.

I would like to express my gratitude to my family, friends and girlfriend, which unconditionally supported me during these months of hard work, giving me the motivation and confidence needed to reach the place that I am now.

My most sincere thanks to my co-supervisor Álvaro Semedo, for his dedicated guidance through this thesis and for sharing with me his extensive knowledge about waves, and the wave climate in particular. Also, a warm thank you word to all the postgraduate studies department personnel, at Escola Naval, for receiving me with open arms and great kindness.

Special thanks to my co-supervisor Pedro Miranda for his advices, patience, and most of all, for being the key-element who gave me the opportunity of working in this field, with all these extraordinary people.

My warm thanks also goes to the COWCLIP community, particularly to Arno Behrens and Joanna Staneva, from *Helmholtz-Zentrum Geesthacht* institute (Germany; former GKSS), for allowing me to use the WAM model simulations, and for co-authoring some of my first scientific works.

# CONTENTS

## List of Figures

full and dashed black lines represent the latitudes of FC21 and PC20 maximum climatological values, for each Hemisphere.

Figure 26 – As in Fig. 25, but for $P_w$.

Figure 27 – FC21F linear trends of $H_S$ (cm/decade) (A) annual, (B) DJF and (C) JJA and $P_w$ (W/m/decade) (D) annual, (E) DJF and (F) JJA.

# List of Tables

# 1. Introduction

Wind waves are ocean surface gravity waves caused by the transfer of momentum from the wind to the water. They are the most energetic ones, accounting for more than half of the energy carried by all waves at the ocean surface (Kinsman, 1965) and thus dominating the ocean wave spectrum, surpassing the contribution of tides, tsunamis, coastal surges, etc. (Munk, 1951). Wind waves (henceforth just called waves for convenience) not only have a direct impact in coastal erosion, but also in sediment transport and beach nourishment, in ship routing and ship design standards, as well as in coastal and offshore infrastructures (Young, 1999), representing a major hazard to any offshore operation or structure and to shipping activity. They are also a part of the climate system, being the "ultimate" air-sea interaction process, clearly visible and noticeable by the human eye, modulating momentum, heat and mass exchanges between the ocean and the atmosphere. Despite their relevance, there is still no precise theoretical model for wave generation and growing processes, considering that the details of such mechanisms are still not fully understood to be accurately quantified. Present third generation wave models rely on the parameterization of the Phillips (1957) and Miles (1957) findings, further modified by Janssen (1991). Nevertheless, wave models have evolved from mainly empirical (first and second generation models) to more physical based ones (present state-of-the art third generation models) (Komen *et al.*, 1994). Third generation wave models are an extremely valuable tool in present time weather forecasting, as well as in research and climate studies. Being important for practical and scientific reasons, a greater understanding of the impact of waves in the climate system is required, and potential changes in future sea state conditions must be considered due to their impacts on the coastal zones and human activities.

Waves are generated by the wind. When wind blows over the sea surface, waves are generated by the momentum transferred downwards to the sea surface. As wind acts over the sea surface, it quickly disturbs the water and forms small ripples. If the wind continues to blow, genuine wind waves will develop. At this stage the sea surface has waves of several lengths (frequencies) receiving energy from the overlaying wind. The wave components of the complex wave field receive this energy and grow until they are saturated. The growth rate of each component is a function of the difference between their phase speed and the wind speed.

Two types of wind waves must be considered at the ocean surface: wind sea and swell. Wind sea waves are young (high frequency, short wave lengths) growing waves that receive

momentum from the wind, being directly connected with the local wind field. These locally generated waves develop very quickly and soon reach their saturation level. Swell waves (lower frequency waves with longer wave lengths), with phase speeds that approach or slightly exceed the wind speed, grow slower, not only from the action of the wind, but also by extracting energy from higher frequency waves due to non-linear wave-wave interactions. Once they propagate away from the generation area (*fetch*) they can divagate freely for thousands of kilometers (Barber and Ursell, 1948; Munk *et al.*, 1963; Snodgrass *et al.*, 1966) with very slight attenuation (Ardhuin *et al.*, 2009). Alves (2006) showed that swell waves can actually propagate across entire ocean basins, until they dissipate their energy upon reaching a coast. For this reason, in the open ocean, the wave spectrum is the result of several wave components, some of them generated locally and some remotely, maybe even several thousands of kilometers away. Hence, it is possible to assume that there is a certain correlation between, for instance, a local coastal erosion event and a storm that took place literally a hemisphere away. This is one of the interesting features (and motivations) that motivate the study of future changes in the global wave climate, since the effect of future climate change in the wind can propagate in the form of wave energy at the ocean surface, and have its impact elsewhere.

During the twentieth century, an atmospheric and oceanic warming trend was observed, as mentioned in the most recent AR5 (Fifth Assessment Report) IPCC (Intergovernmental Panel on Climate Change) report (IPCC, 2013). Anthropogenic emissions of greenhouse gases have consensually been assumed as the cause for such trends that will still be present towards the end of the twenty-first century due to further greenhouse gases emissions (Solomon *et al.*, 2007) and to the inertia of the climate system. The expected global warming for the twenty-first century will lead to changes in the close to the surface wind speeds, and therefore on the future wave climate. With the goal of studying the impact of the expected changes in the future climate, under the auspices of the Coordinated Ocean Wave Climate Project (COWCLIP), several global wave climate projections (dynamical and statistical) were recently published in the scientific literature (e.g. Mori *et al.*, 2010; Semedo *et al.*, 2013; Hemer *et al.*, 2013a; Fan *et al.,* 2013; Wang *et al.*, 2015; Erikson *et al.*, 2015). These simulations had, as wind and sea ice forcing, CMIP3 (Coupled Model Inter-comparison Project, phase 3) global climate models (GCM) projections, and followed the main recommendation of the first COWCLIP workshop (Hemer *et al.*, 2013a), which stressed the need of coherent global ocean wave climate projections, since the impact of global warming on future wave climate had been practically ignored in the IPCC AR4 report (IPCC, 2007).

The results from these simulations, as mentioned in the IPCC AR5 report, have shown a consistent future climate change in the mean wave climate, with increases in wave heights over the Southern Ocean, and decreases in the subtropics and in the North Atlantic sub-basin, as well as anticlockwise rotations of mean wave direction in the northern side of the extratropical storm belts, associated with projected poleward shifts of the storm tracks, resulting from losses in the polar sea ice extent (Hemer *et al.*, 2013a). All the CMIP3 COWCLIP global wave climate simulations were based on the AR4 emission scenarios (Hemer *et al.*, 2012). To our knowledge, very few wave climate simulations based on CMIP5 can be found in the scientific literature: Dobrynin *et al.*, (2012), Dobrynin *et al.*, (2015), and Hemer *et al.*, (2015) are the exceptions.

The present study main goal is to describe the impact of climate warming in the global future wave climate towards the end of the twenty-first century, based on a 2-member "coherent" ensemble of wave climate CMIP5 projections. These two wave climate projections were produced by a single wave model (WAM; WAMDI group, 1988), forced (wind and sea ice) by two climate simulations from the EC-Earth GCM, with the same scenario (Representative Concentration Pathway 8.5 – RCP8.5), making the 2-member ensemble a single model (WAM), single forcing (EC-Earth), and single scenario (RCP8.5) "coherent" simulation. The wave data consists of two major sets of 6-hourly global fields with a 1º x 1º grid resolution, with a total span of 130 years. The present climate simulations cover the period from 1971 to 2005 (historic period) and the future climate runs span from 2006 to 2100. The future changes in the global wave climate were analyzed for the 2071-2100 period, and compared to the 1971-2000 present climate period. The historic period was validated with *in-situ* buoy observations and with the ECMWF (European Centre for Medium-Range Weather Forecasts) ERA-Interim reanalysis (Dee *et al.*, 2011) wave data.

In spite of the wind waves predominance in the global oceans' surface, and their influence in different human activities, long term analysis of wave climate are relatively limited, relying on *in situ* observational records (approximately 40 years in length), satellite altimeter records (25 years in length) and wave modeling reanalysis, typically within 30 to 40 years in length, like for example the ERA-40 (45 years; Uppala *et al.*, 2005; Sterl and Caires, 2005; Semedo *et al.*, 2011) or the ERA-Interim (from 1979 onwards; Dee *et al.*, 2011), being these reanalyzes produced by the ECMWF. Such short records lead to difficulties regarding detection and attribution of natural long term (decadal) variability and change in the wave climate system. This situation was however assessed in the IPCC AR4 report, but only in terms of wave heights. Although observations from voluntary observing ships (VOS; e.g.,

Gulev *et al.*, 2003) are longer, they have a very narrow spatial coverage, depending on the ship routes, that naturally tend to avoid locations with extreme conditions, resulting in under representation of the high sea states in the data set (Young, 1999). Since these data sets are a result of human observation, many sources of random and systematic errors have also been found (Gulev *et al.*, 2003). They are, nevertheless, one of the vastest sources of oceanographic information, detaining the longest continuity between sets since the beginning of the twentieth century. VOS data have also been used to compile global wave statistics (Hogben and Lumb, 1967; Hogben *et al.*, 1986) but, as mentioned before, it needs to be treated very carefully. For these reasons, global wave climate data with a full spectral description of the ocean surface needs, at present, to rely mostly on wave modeling sets, like reanalysis or hindcasts.

This thesis intends to describe the impact of future climate warming in the twenty-first century wave climate, using a 2-member "coherent" ensemble of wave climate projections: single wave model (WAM), single GCM forcing (EC-Earth), and single scenario (RCP8.5). The document is organized as follows: firstly, in Chapter 1, the data sets and methodologies used are discussed. In Chapter 2, a description of the model is presented, and it's capability to represent the present wave climate is assessed. Chapter 3 provides a description of the impact of climate change (global warming) on the global wave climate. In Chapter 4, an EOF analysis for the North Atlantic's sub-basin is shown, as well as a present-future meridional climatological comparison for three different sub-basins. Chapter 5 presents a final decadal tendency study, and lastly the main conclusions of this work.

## 2.    Data and Methods

### 2.1    Wave model WAM

The wave model WAM (WAMDI Group, 1988) is a third generation wave model, developed during the 1980s, with the important goal of producing an operational model to forecast waves over the whole globe. The WAM model is forced by a wind field at the height of 10 m, and resolves the so called *action balance equation* (eq. (1); Mei, 1983; Komen *et al.*, 1994), with no previous assumptions of the wave spectral shape. WAM outputs a two dimensional wave energy spectrum *F(f,θ)*, that describes how the mean sea surface elevation variance is distributed as a function of *f* (frequency) and *θ* (direction of propagation):

$$\frac{\partial}{\partial t}F(f,\theta) + \nabla.\left(c_g F(f,\theta)\right) = S_{in} + S_{ds} + S_{nl} + S_{bot} . \quad (1)$$

Equation (1) describes the evolution of the wave energy spectrum as the sum of the local wind input ($S_{in}$), wave dissipation due to wave breaking ($S_{ds}$), non-linear wave-wave interaction ($S_{nl}$), and an additional term that accounts for energy loss due to bottom friction ($S_{bot}$), that works only in shallow waters. Considering the total sea surface state in a certain location and time, as the result of superposition of many wave components, differing in height, frequency, wave length and direction, the use of an energy spectrum is the best approach to describe that surface, changing continuously over time (Koeman *et al.*, 1994). From this spectrum, several integrated wave parameters can be obtained from the spectral momentums (eq. (2)), such as the significant height ($H_S$; eq. (3)) and mean period ($T_m$; eq. (4)) (Bidlot *et al.*, 2007). The *nth*-order moment of the spectrum is defined as:

$$m_n = \iint f^0 F(f,\theta) df d\theta. \quad (2)$$

The significant wave height $H_S$ is obtained as:

$$H_S = 4.04\sqrt{m_0} , \quad (3)$$

and the mean wave period $T_m$ is computed as:

$$T_m = \frac{m_0}{m_1}. \quad (4)$$

The mean wave direction (MWD) is defined as $\theta_m = \mathrm{atan}\,(SF/CF)$, where:

$$SF = \iint \sin\theta\, F(f,\theta)df d\theta, \text{ and} \quad (5)$$
$$CF = \iint \cos\theta\, F(f,\theta)df d\theta. \quad (6)$$

Over time, upgrades to WAM have been developed, and recently it received more improvements, including an adjusted formulation of the ocean wave dissipation scheme, and a new form of parameterization of unresolved bathymetry (Bidlot *et al.*, 2007).

The two wave climate ensemble members, produced with the WAM model, correspond to simulations nr. 1 and nr. 4 (from a total of 8) of a larger COWCLIP ensemble (8 dynamical members, plus 20 statistical members) – GLOWAVES-2. These two members were forced by wind speed and sea ice coverage CMIP5 EC-Earth runs from the *Instituto Dom Luiz* - University of Lisbon (member 1), and the Swedish Meteorological and Hydrological Institute (SMHI; member 4) following the representative concentration pathway with a high emissions scenario 8.5 (RCP8.5). The wave data consists of two major sets of 6-hourly global fields with a 1°×1° grid resolution, with a total span of 130 years (1971-2100: present climate, 1971-2005 and future projection, 2006-2100). Latitude ranges from 78°S to 78°N (in order to avoid the polar areas) but for analysis purposes the interval was confined to 75°S–75°N. The spectral domain ranges from 0.041 to 0.411 Hz, corresponding to wavelengths of about 10-950 m. Directions of propagation were represented using a resolution of 15°.

## 2.2 EC-Earth global climate model forcing

The EC-Earth model is a full physics seamless atmosphere-ocean-sea-ice coupled earth system prediction model (Hazeleger *et al.*, 2010). It was developed from a version of the operational seasonal forecast system of ECMWF. The two GCM simulations that provided the forcing to the WAM runs, used the EC-Earth version 2.2, which is based on the ECMWF seasonal forecast system 3. The atmospheric model in EC-Earth is the ECMWF IFS (Integrated Forecast System) cycle 31r, with a set-up corresponding to the use of a horizontal spectral resolution of T159 (triangular truncation at wavenumber 159) (roughly 125 km), with

62 vertical levels of a terrain following mixed sigma-pressure hybrid coordinates, about 15 of which within the planetary boundary layer. The ocean model in EC-Earth version 2.2 is the NEMO (Nucleus for European Modeling of the Ocean; Semedo *et al.*, 2015), with a horizontal resolution of approximately 1°×1°.

## 2.3    ERA-Interim data

ERA-Interim wave data was used to evaluate the performance of the two GLOWAVES-2 simulations during the present climate time slice in terms of wave heights, mean wave periods, and wave energy flux (power). The ERA-Interim is a global ECMWF third generation reanalysis (following the previous ERA-40, and the first ERA-15 reanalyzes) covering the period from 1 January 1979 until the present day (continuing to be extended in almost real time). A reanalysis can be described as a systematic approach to produce data sets for climate monitoring and research, being created via unchanging data assimilation of all the available observations over the analyzed period, with the same model(s). Consequently, it provides a complete dataset that is as temporally homogeneous as possible. Naturally, due to uneven data coverage and changes in the observation systems some inhomogeneities are still present (Uppala, 1997; Sterl, 2004), but biases have steadily improved.

ERA-Interim uses an improved assimilation system (4DVAR - 4D variational data assimilation) correcting several of the inaccuracies exhibited by ERA-40, despite the same input observational records, until 2002. Besides atmospheric variables, ERA-Interim also includes wave parameters, since it was produced using the IFS release cycle Cy31r2, a two-way coupled atmosphere-wave model system (Janssen, 2004). The wave model used in this coupled system is the WAM model. The atmospheric parameters that influence wave growth are passed to the wave model, and this returns information about the impact on sea surface roughness via the Charnok parameter (Janssen, 1991, 2004). Notable improvement of ERA-Interim significant wave heights and mean wave periods relative to ERA-40 were reported by Dee *et al.* (2011). Although the original resolution of the atmospheric parameters in ERA-Interim is of about 80 km (T255 spectral truncation; ~0.7°), WAM is applied with a horizontal resolution of 110 km so, (~ 1°×1°). Once again, for analysis purposes, the latitude range was confined to 75ºS–75ºN. Additional details about the ERA-Interim reanalysis can be found in Dee and Uppala (2009) and Dee *et al.*, (2011).

## 2.4 Buoy data

H$_S$ data was validated against observations of 8 *in situ* buoys in the northeast Atlantic (see Figure 1 and Table 1), from different institutions, such as Puertos del Estado (Spain; 2 buoys), Marine Institute & Met Eireann (Ireland), UK Met Office (United Kingdom) and Meteo France (6 buoys), spreading along the Eastern half of the North Atlantic Ocean. The buoy data were time averaged and collocated with simulations and reanalysis data in the form of histograms (with fit curves) and scatter plots (annual means for each buoy). Time constraint was ignored in histogram assembly, since WAM (and the EC-Earth) runs were not subjected to data assimilation, and thus they are considered representative of the current climatological mean atmospheric and wave climates regardless of the time period.
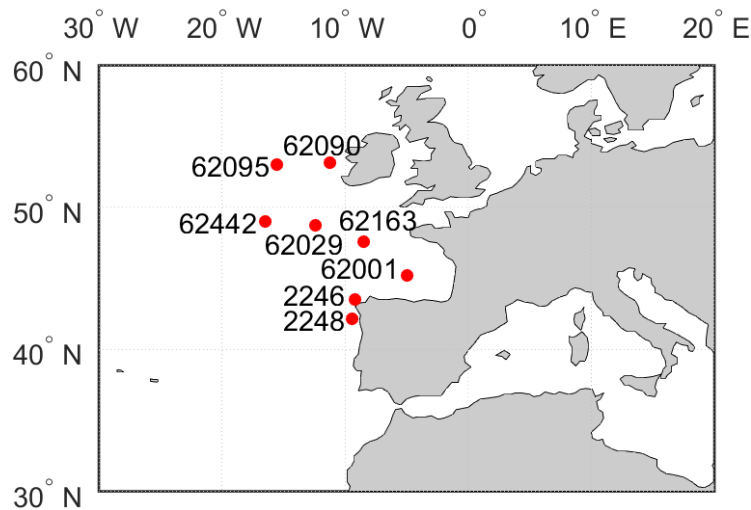


*Figure 1 – Buoys: the red dots represent the position of each buoy, numbered in accordance with its WMO (World Meteorological Organization) code identifications.*

*Table 1 – Detailed buoy data: along the "Owner" column, MO – Met Office (UK), MI – Marine Institute (Ireland), ME – Met Eireann (Ireland), MF – Meteo France.*

| BUOY name | Nº (station) | Latitude (º) | Longitude (º) | Depth (m) | Owner | Period |
|---|---|---|---|---|---|---|
| K1 | 62029 | 48.720 | -12.430 | *NA\** | MO | 2006-2016 |
| Pap | 62442 | 49.000 | -16.500 | *NA\** | MO | 2010-2016 |
| M1 | 62090 | 53.127 | -11.200 | 140 | MI & ME & MO | 2002-2007 |
| M6 | 62095 | 53.000 | -15.530 | 3000 | MI & ME & MO | 2006-2016 |
| C. Silleiro | 2248 | 42.120 | -9.430 | 600 | Puertos del Estado | 1998-2016 |
| V.-Sisargas | 2246 | 43.500 | -9.210 | 386 | Puertos del Estado | 1998-2016 |
| Gascogne | 62001 | 45.230 | -5.000 | *NA\** | MO & MF | 2002-2012 |
| Brittany | 62163 | 47.550 | -8.470 | *NA\** | MO & MF | 2002-2012 |

*\*NA:* data not available.

## 2.5    Methodology and wave parameters

The present wave climate (historic; PC20), used as reference to assess the future wave climate changes, is computed as the mean of the two ensemble members PC20-1 and PC20-4 present wave climates, the historical periods of the GLOWAVES-2 ensemble members numbers 1 and 4, respectively. The historical ensemble wave climate simulations (PC20-1 and PC20-4), covers the period from 1971 to 2005. The ensemble future wave climate projection (FC21), computed as the mean of the two ensemble members projections (FC21-1 and FC21-4), covers the period from 2071 to 2100 (30 years). For coherence, the present climate historical period used in the present thesis ranges from 1971 to 2000 (also 30 years). The projected impact of climate change on future wave climate is assessed by comparing PC20 with FC21. Projections include values of $H_S$ (significant wave height; m), formerly defined by Munk (1944) as the mean wave height of the highest one-third of all waves in record, or four times the standard deviation of the surface elevation, $T_m$ (mean period; s), MWD (mean wave direction (propagation from); °) and $P_w$ (wave power; W/m, $= (\rho g^2/32\pi)\,T_m\,H_S{}^2$, as in Young, 1999). To back up these results, $U_{10}$ (near-surface marine wind speed, at 10 meters height; m/s) projections were also generated. The impact of climate change on these parameters (comparison between PC20 and FC21; the main focus of this thesis) is assessed through several different approaches: firstly, a simple juxtaposition between the global distribution of each field, obtaining the normalized differences (for $H_S$, $T_m$ and $P_w$) or anomalies (for MWD) between the present and future climate sets. Subsequently, an EOF analysis is presented, in order to assess the main changes in the positions of the $H_S$ and $P_w$ centers of action. To back up these results, meridional cross sections for $H_S$ and $P_w$ are displayed, where the impact of climate change is observable, as in the parameters' absolute values, as in their latitudinal shifting. The 6-hourly wind and wave parameters were processed for annual and seasonal means (winter and summer seasons: DJF (December, January and February) and JJA (June, July, August)).

In the high latitudes, natural variations of ice cover extent can seriously affect the quality of mean wave fields, due to a considerable reduction of data points available, as sea ice is taken as land by the model. This situation was dealt by using one of the procedures proposed by Tuomi *et al.* (2011), where each grid cell with a 30% or more ice concentration in the scrutinized periods was coded as a land point, leaving only cells with 70% or more of the total time series to be treated as open water.

# 3.    Wave model validation

In order to have confidence in the wave model long-term future climate simulations, it is crucial to assess the model capability to represent the present wave climate. As mentioned in section 2, ensemble members (PC20-1 and PC20-4) means (of $H_S$, $T_m$, and $P_w$) from 1971 to 2005 are compared to ERA-Interim means from 1979 to 2013. The ensemble members are also compared to *in situ* buoy observations of $H_S$ from 8 different locations along the Eastern North Atlantic.

## 3.1    Comparison with ERA-Interim reanalysis

Fig. 1 displays the annual $H_S$ means for ERA-Interim and the two present climate datasets. Maximum climatological values of $H_S$ are present in the midlatitudes of both hemispheres, being the highest ones in the Southern Ocean Indian sector, surpassing 5 m. There is an obvious similarity between the ensemble and ERA-Interim patterns, yet some slight differences are noticeable.

The annual $H_S$ anomalies (differences between PC20-1,4 and ERA-Interim), and the normalized differences (PC20-1,4 minus ERA-Interim normalized by ERA-Interim) are shown in Fig 3.
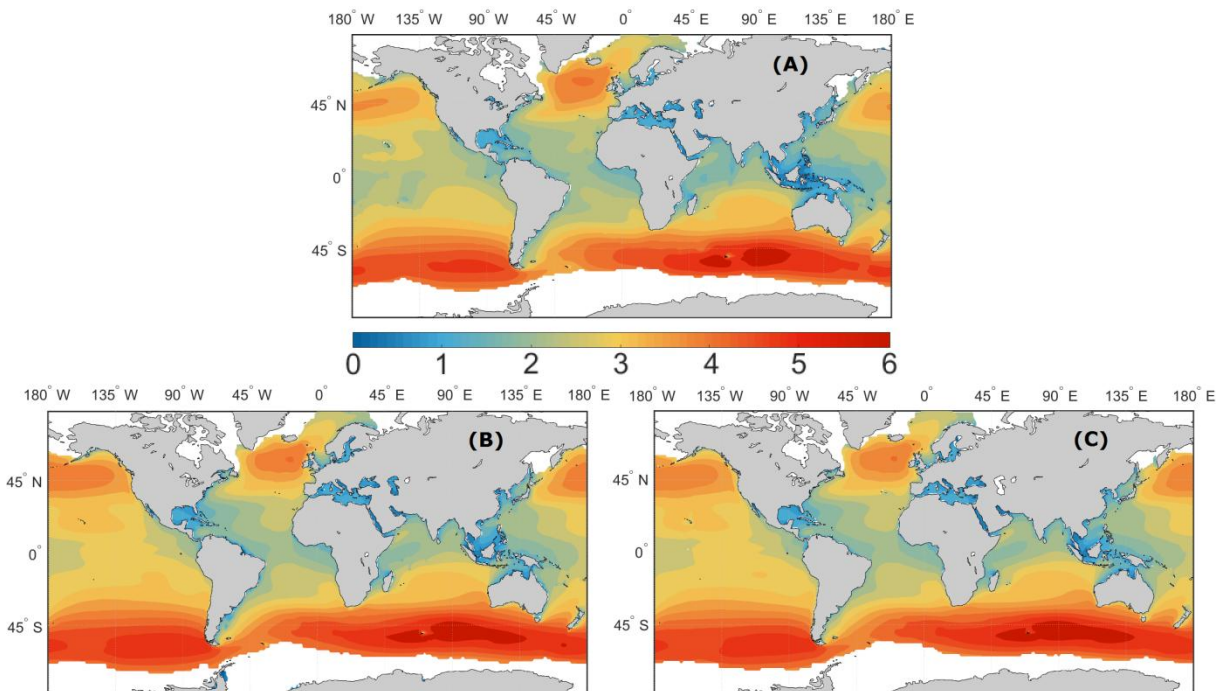


*Figure 2 – Annual means of $H_S$ (m), 1979-2013 for (A) ERA-Interim, and 1971-2005 for (B) PC20-1 and (C) PC20-4.*

Ensemble members PC20-1,4 overestimate $H_S$, when compared to ERA-Interim, in most of the global ocean, with higher anomalies (Figs 3a,b) along the tropical regions of the Pacific Ocean: ~40-50 cm (~15-20 %; Figs. 3c,d). Positive anomalies for PC20-1,4 can also be found in the North Pacific sub-basin (~10-15%), and in the Southern Ocean (Indian, Pacific, and Atlantic sectors; less than 7%). Exceptions are in the western half of the Atlantic Ocean basin, where the reanalysis wave height values are higher, especially in the low and tropical latitudes (but less than 10%). Differences tend to be substantially lower along the main climatological wave generation areas, in the extratropical latitudes (Young, 1999): in the North Atlantic sub-basin extratropics, for instance, PC20-1,4 underestimates (overestimates) $H_S$, compared to ERA-Interim, in the western (eastern) area by less than 5 %.

The seasonal differences (absolute and normalized; for December – February (DJF) and June – August (JJA); not shown – see supplementary material) are of the same order of magnitude, apart from the equatorial region of the Indian Ocean basin in DJF, where they can reach almost 40% (~50 cm), and the in the Southern Ocean Pacific and Indian sectors, in JJA, where the anomalies are slightly negative (~10 cm or less than 5%).
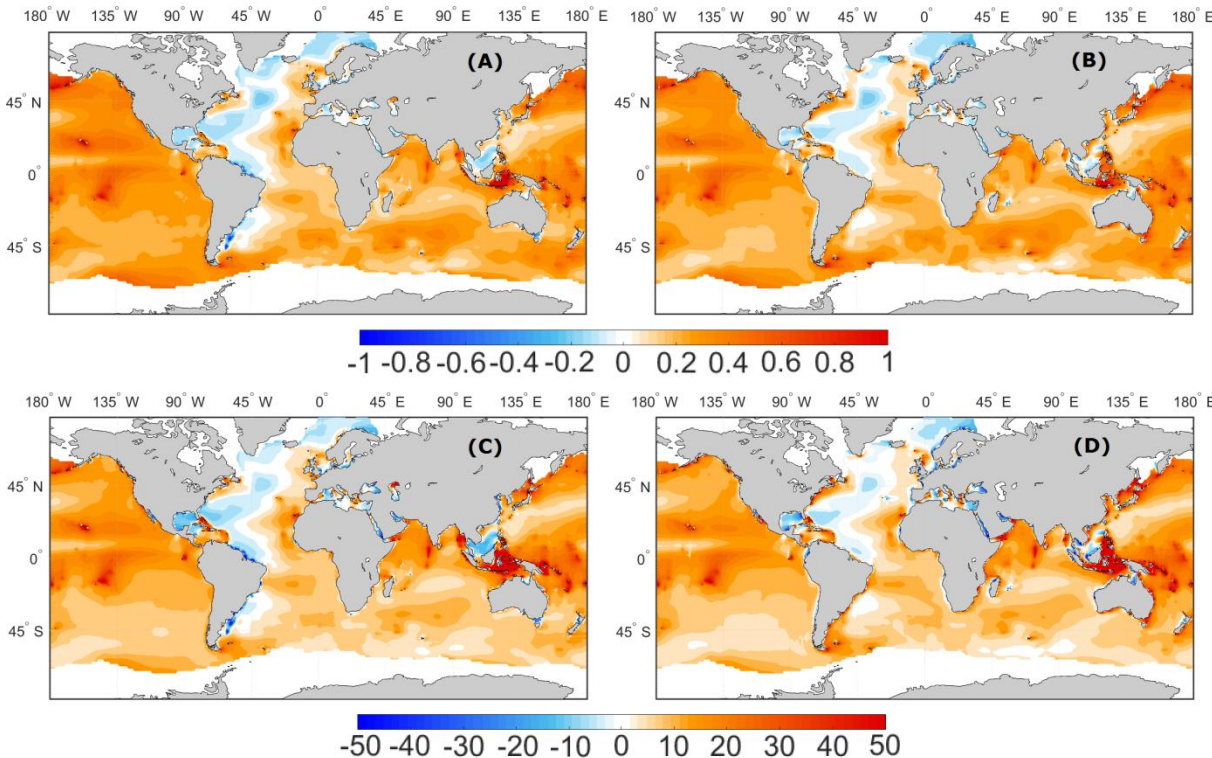


*Figure 3 – Anomalies (m) between simulations and reanalysis ((A), PC20-1, and (B), PC20-4) and the respective normalized differences (%) ((C), PC20-1, and (D), PC20-4).*

The same kind of analysis was produced for the mean wave period $T_m$. Fig. 4, as Fig. 3, shows the annual $T_m$ means for ERA-Interim, and the two present climate simulations datasets. Here, the maximum values take place over the tropical and subtropical regions of the eastern half of the Pacific and Indian oceans' sub-basins. This pattern is explained taking into account the swell propagation and growth (in wavelength and period) from the Southern Ocean, northwards (Young, 1999; Alves, 2006; Semedo *et al.*, 2011). Anomalies (in s) and normalized differences (in %) are presented in Fig. 5.

Just as for $H_S$, PC20-1,4 slightly overestimates the wave periods on a global scale, typically within 5%-10% (1-2 s). However, the negative wave height differences previously found in the Atlantic Ocean no longer take place. In fact, the North Atlantic sub-basin is the best represented region for $T_m$, with a very satisfactory agreement between the ensemble members and reanalysis. In the North Pacific sub-basin extratropics, differences reach up to 10% (~2 s), but these tend to be lower in the Southern Ocean (less than 7% (~1 s)). Tropical regions still detain the largest heterogeneities, along the so called "swell pools", where waves are typically smaller and longer (Chen *et al.*, 2002; Semedo *et al.*, 2011), locally reaching 15% (~2 s). Seasonally (not shown; see supplementary material), discrepancies from the annual mean patterns are more evident for JJA in the North Atlantic Ocean, where a minor overestimation can be found (up to 5%, ~1 s).
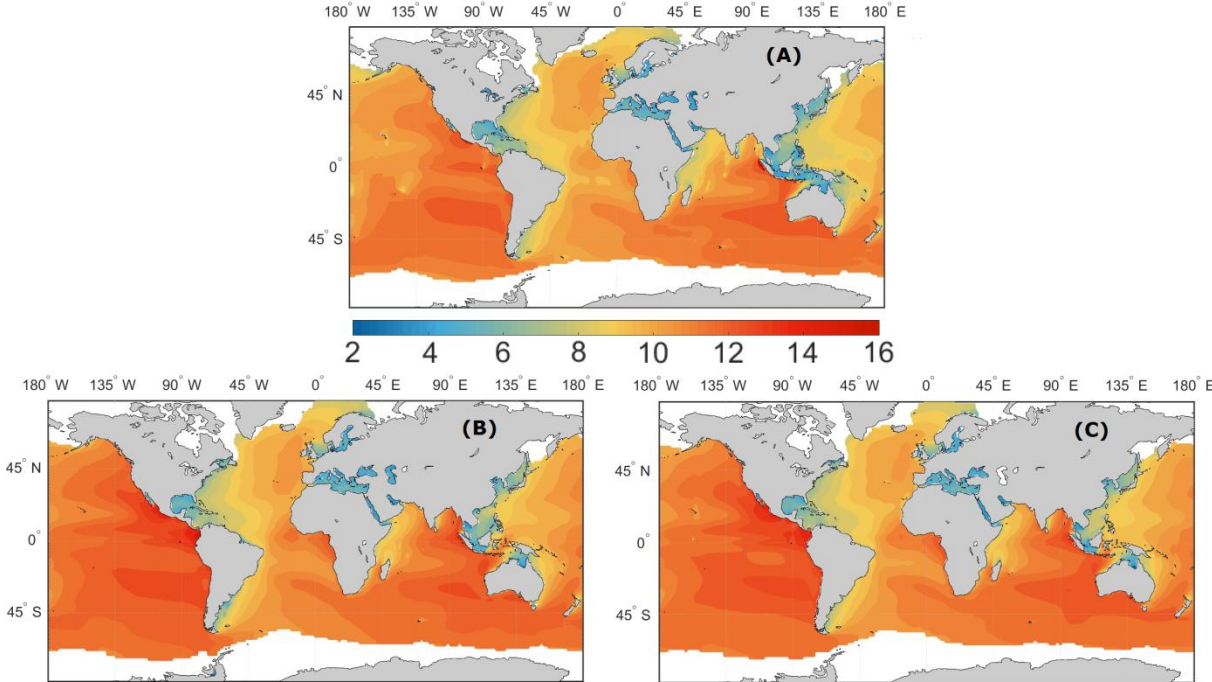


*Figure 4 – As in Fig. 2, but for $T_m$ (s).*
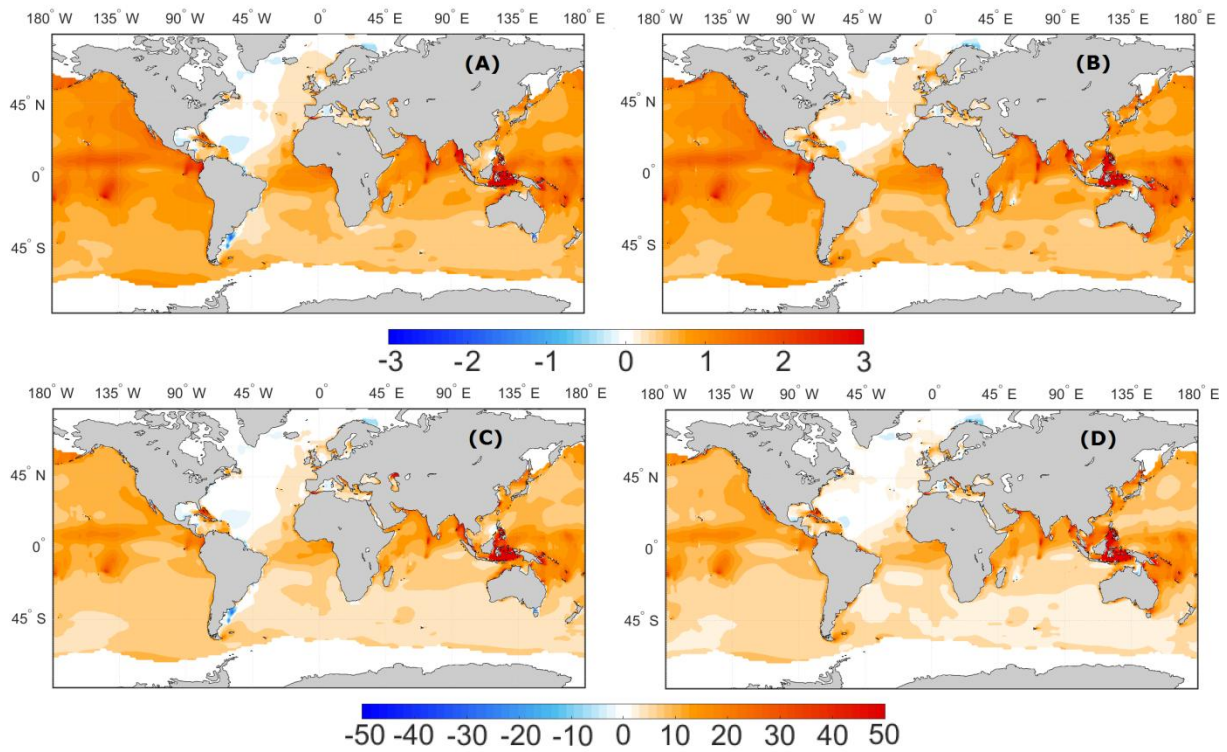
*Figure 5 – As in Fig. 3, but for $T_m$ (s).*

Both in $H_S$ and $T_m$ maps, higher differences are present in some coastal zones (e. g. along the coast of Argentina) and archipelagos (Indonesia, Caribbean, Hawaii, French Polynesia, etc.), mostly due to land mask differences between the wave climate simulations (PC20-1,4) and ERA-Interim, and not the wave model itself.

The annual PC20-1,4 $H_S$ and $P_w$ histograms are displayed in Figure 6. The global distributions (of frequency of occurrence) were computed from the correspondent annual means. Each bar corresponds to a 0.25 m and to 10 W/m interval for wave height and power, respectively. A fit curve is overlaid in the respective $H_S$ and $P_w$ histograms. The same global analysis was performed for the seasonal means (not shown; see supplementary material), as well as for three different basins (Atlantic, Pacific and Indian oceans; also not shown), separately.
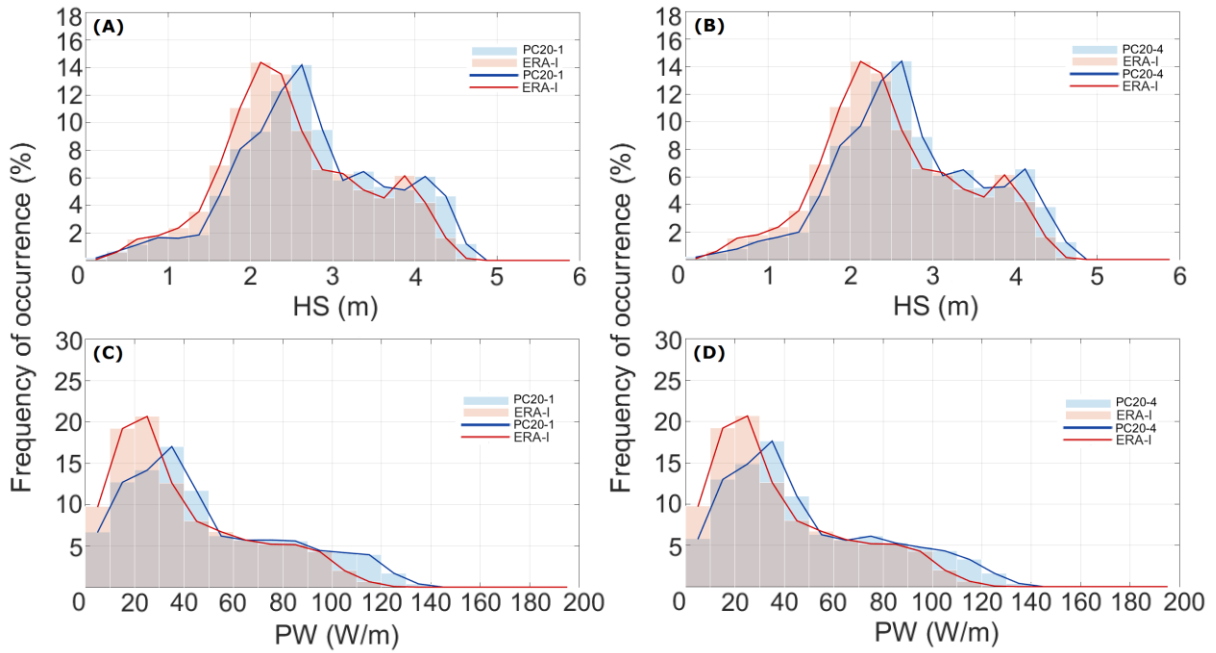
*Figure 6 – Histograms and fit curves (%) of (A and B) $H_S$ (m) and (C and D) $P_w$ (W/m), computed from global annual means of PC20-1,4 (blue lines) and ERA-Interim (red lines), for (A and C) PC20-1 and (B and D) PC20-4.*

As seen before, the PC20-1,4 overestimation for $H_S$ can be observed through the right-shifted blue histograms, dominating the highest values (wave heights above 2.5 m). Similar behavior is detected for $P_w$, with an even more pronounced ERA-Interim prevalence in the lowest values (below 30 W/m). The sector 50-100 W/m seems to be well represented in both PC20-1 and PC20-4, though. Seasonally (not shown; see supplementary material), JJA presents a better agreement between the global histograms for both $H_S$ and $P_w$ with identical frequencies of occurrence for the 2.8-4 m and 40-90 W/m intervals, respectively. It's also in the austral winter that the highest values for both variables tend to occur.

Fig. 7 displays the magnitude of the $H_S$ annual and seasonal (DJF and JJA) interannual variability bias of PC20-1,4 in relation to ERA-Interim, by comparing the variances of the yearly mean values of the datasets ($r = \sigma_{CR}{}^2/\sigma_{EI}{}^2$). Due to the its large range of values, a binary logarithm was applied to the previously defined ratio. Hence, the ensemble members underestimate variances where $log_2(r) < 0$ and overestimate them where $log_2(r) > 0$. If $log_2(r) = 0$, then $r = 1$ and both variances are identical.
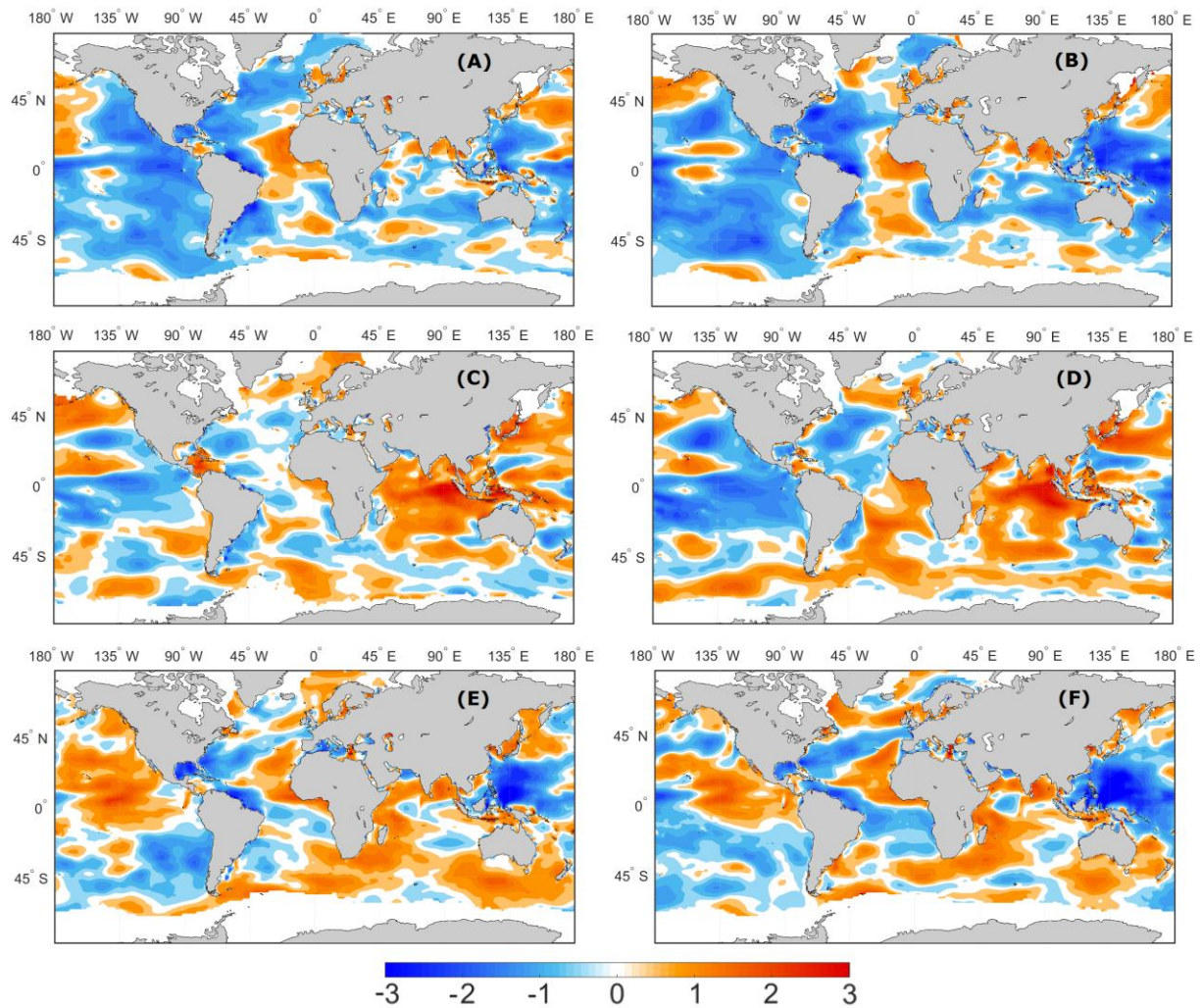
*Figure 7 – Interannual ((A) and (B)) annual, ((C) and (D)) DJF and ((E) and (F)) JJA Hs variability bias (dimensionless) between the PC20-1 (left) and PC20-4 (right), and ERA-Interim variances.*

On an annual scale, it is visible that the simulations tend to underestimate variability mainly across the Pacific Ocean, but also in the western half of the Atlantic sub-basin. Globally, this undervaluation is set on 23% for PC20-1 and 27% for PC20-4. On the other hand, in DJF, there is a considerable overestimation across the tropical and subtropical regions of the Indian Ocean. Nevertheless, the Atlantic Ocean is very well represented in PC20-1 (Fig. 7c), and global values put the two ensemble members above the reanalysis at just 9% and 4%, correspondingly. In JJA, a moderate amplification of reanalysis values can be found for the Pacific and Atlantic equatorial regions. Also during this season, as PC20-1 slightly overestimates the global mean variability, in just 3% (best result), PC20-4 undervalues it in 5%.

## 3.2 Comparison with buoy data

The results of the validation of the PC20-1,4 $H_S$ values against buoy observations are presented in Fig. 8. The scatter-plots (Figs 8a,b) compare the annual mean $H_S$ buoy observations (using only years with at least 90% coverage) with PC20-1,4 annual mean $H_S$ values (for the selected correspondent years). Linear trends were computed for each comparison. An equivalent analysis was performed for $H_S$ buoy observations and the ERA-Interim reanalysis (not shown, but the resulting linear trend is present). In Fig. 8c, the mean histograms for buoy observations (computed from the 8 buoys), PC20-1,4, and ERA-Interim are shown, with the respective fit curves. Each bar corresponds to a 0.25 m interval, for wave height, as in Fig. 6.
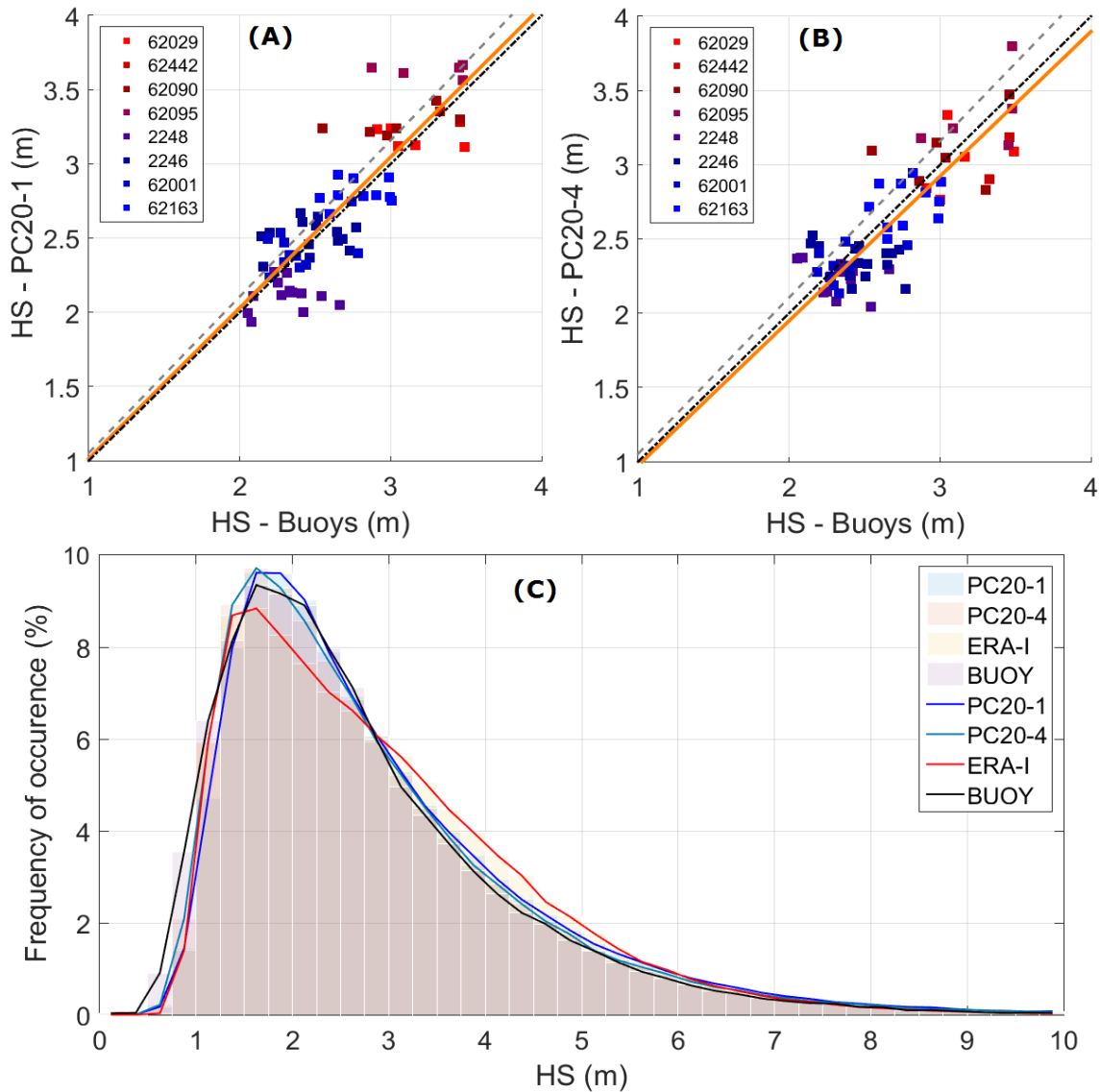


*Figure 8 – Scatter-plots of buoys annual means (of at least 90% complete years) versus (A) PC20-1 and (B) PC20-4 annual means for the same location and yearspan, with linear trends (orange lines; and from the comparison of buoys with ERA-Interim data: dashed gray lines). (C) Histogram and fit curve from buoy observations (black line), PC20-1,4 (blue and light blue lines) and ERA-Interim reanalysis data (red line).*

The results are very satisfactory. In the set of years used to perform the scatter-plot analysis, PC20-1 tends to slightly overestimate buoy wave height (in 1.54% on average), while PC20-4 lightly underestimates it (in 2.57% on average), both below the bias found in the comparison with ERA-Interim (dashed gray lines; +5.29%), maybe because the model incorporates the complete swell history. The agreement between buoy observations and the simulations is visible through the correlation coefficients of the referred scatterplots: 0.84 to the first one (Buoys *vs* PC20-1) and 0.82 to the second one (Buoys *vs* PC20-4). This consistency is also visible in the histograms present in Fig. 8c, that are rather similar. Both the simulations and the reanalysis tend to underestimate $H_S$ buoy observations below 1 m, though. There is also a mild overestimation for heights above 3 m, nevertheless, this anomaly is dominated by ERA-Interim, differing from what was observed before (in Fig. 6a,b), and probably related to the use of a distinct (spatially restricted) data set, due to the specific location of the buoys. Altogether, the juxtaposition between the two PC20-1,4 ensemble members and the buoy observations show a strong agreement among the sets, with absolute wave height mean differences (mean of PC20-1,4 minus mean of the 8 sets of buoy observations) of +21.20 cm for PC20-1 and +12.60 cm for PC20-4.

The general agreement between the historical ensemble members and the reanalysis (better than in Semedo *et al.*, 2013 and in Hemer *et al.*, 2013a), and the historical ensemble members and *in situ* buoy data, shows that the WAM model, forced with the wind speed and sea ice cover from EC-Earth projections, produces realistic scenarios of the global wave climate at the end of the twentieth century. This gives the necessary confidence in the ability of the WAM model to simulate a realistic climate change signal towards the end of the twenty-first century.

# 4.    Impact of future climate change on global wave climate

Considering the capability of the wave model WAM, forced by EC-Earth, to simulate the global present wave climate, this section describes the projected changes in $H_S$ (and wind speed at 10 meters height $U_{10}$), $T_m$, MWD and $P_w$, between the present climate (PC20; 1971-2000) and the future climate (FC21; 2071-2100), on an annual and seasonal (DJF and JJA) scale. Results shown in the following figures correspond to the mean of the two GLOWAVES-2 ensemble members (PC20 is the mean between PC20-1 and PC20-4, and FC21 is the mean between FC21-1 and FC21-4). The statistical significance of these projected changes is assessed using a standard *t*-test for difference in means, which determines if the present and future climates are statistically different from each other, for every grid point. The shaded areas in further normalized differences maps (between FC21 and PC20: FC21 minus PC20 normalized by PC20) refer to statistically non-significant (at 95% confidence level) altered regions.

## 4.1    Significant wave height ($H_S$) and surface wind field ($U_{10}$)

The PC20 and FC21 annual $H_S$ means, along with the correspondent normalized difference between future and present climates (FC21 minus PC20 normalized by PC20) are exhibited in Fig. 9. The long-term $H_S$ projection (FC21; Fig. 9b) shows the highest wave height values along the extratropical storm tracks of each hemisphere, and lowest in the lower latitudes and sheltered *fetch*-limited areas (e.g. Gulf of Mexico, Mediterranean Sea, Indonesia, etc.), similarly to the present climate pattern. Although, there is a visible and statistically significant projected increase (Fig 9c) covering all the Southern Ocean (reaching approximately 15%, and as far as 90 cm locally), and along the eastern equatorial and southern subtropical regions ("swell pools") of the East Pacific Ocean (up to 5%; ~15 cm). A clear projected decrease in the North Atlantic Ocean (up to 10%, or ~40 cm, south of Iceland) is also noticeable. Non-statistically significant $H_S$ increases can be expected for the South Atlantic Ocean, especially along the coast of Africa (Gulf of Guinea), and for the Arabic sea, Bay of Bengal, Andaman Sea and Gulf of Thailand, in the Indian Ocean.
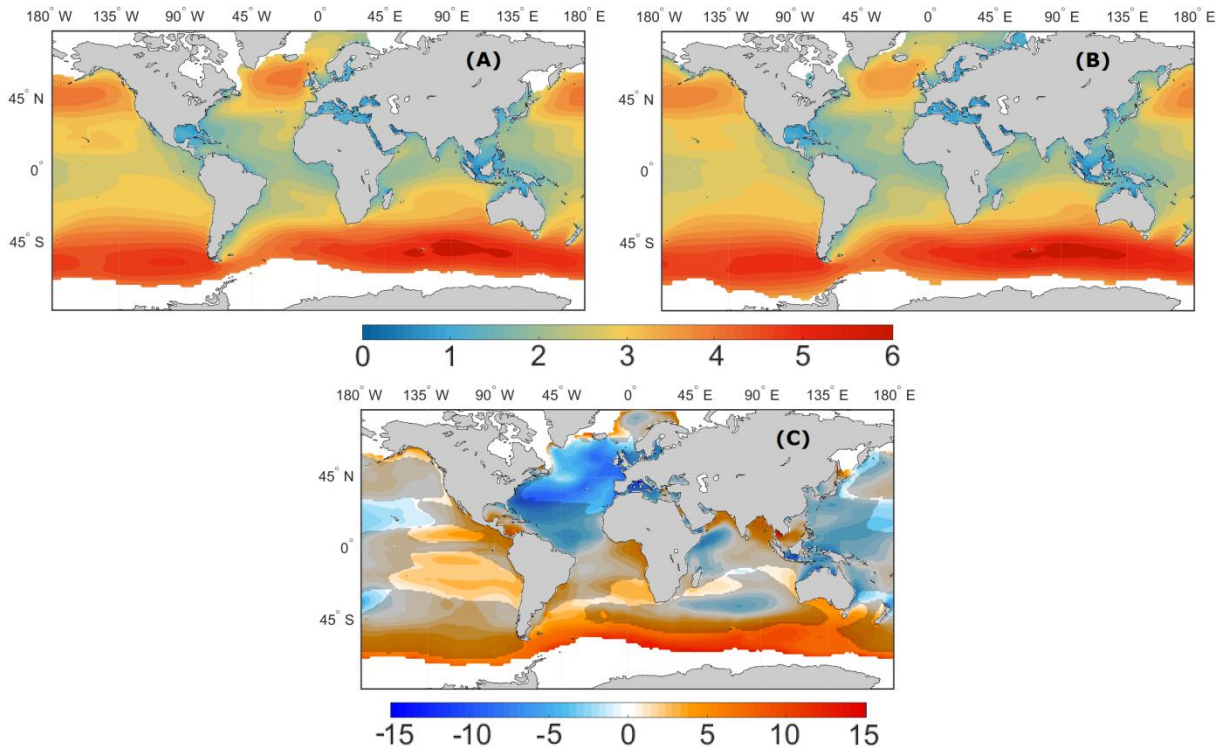
*Figure 9 – Annual means of $H_S$ (m), for (A) PC20 and (B) FC21, and (C) $H_S$ normalized differences (%): FC21 minus PC20 normalized by PC20.*

From a seasonal perspective (Figs. 10 and 11), wave height maximum mean values are higher in the respective winter hemisphere. The mean wave height amplitude between seasons (DJF and JJA) is more pronounced in the Northern Hemisphere, reaching almost 4 m, while it hardly surpasses 2 m in the Southern Hemisphere, due to the constant strong winds in the midlatitudes, blowing almost unimpeded by any land mass, and generating a more stable wave field in the Southern Ocean.

The DJF PC20 and FC21 $H_S$ means, and the correspondent normalized differences between future and present climates are shown in Fig. 10. During DJF, the major statistically significant decreases in wave heights are projected to take place in the North Atlantic sub-basin, mainly between 5% to 10% (10-30 cm), but reaching 15% south of Iceland (~80 cm). Considerable decreases are also to be expected in Indonesia and all its surroundings (Indian Ocean and West Pacific Ocean; Fig. 10c). Relevant (and statistically significant) projected increases in $H_S$ are visible for the West Pacific Ocean, less than 7% in the tropical and subtropical regions, but higher (7-10%) in the mid-to-high latitudes, peaking along the coast of Alaska and the Drake Passage, in Antarctica, most possibly due to the retraction of the sea ice cover extent, creating additional free space to wind-sea interactions and wave growth. The

same happens in the high latitudes of the North Atlantic Ocean (e.g. along the east coast of Greenland) but in smaller scale due to geographic conditioning.
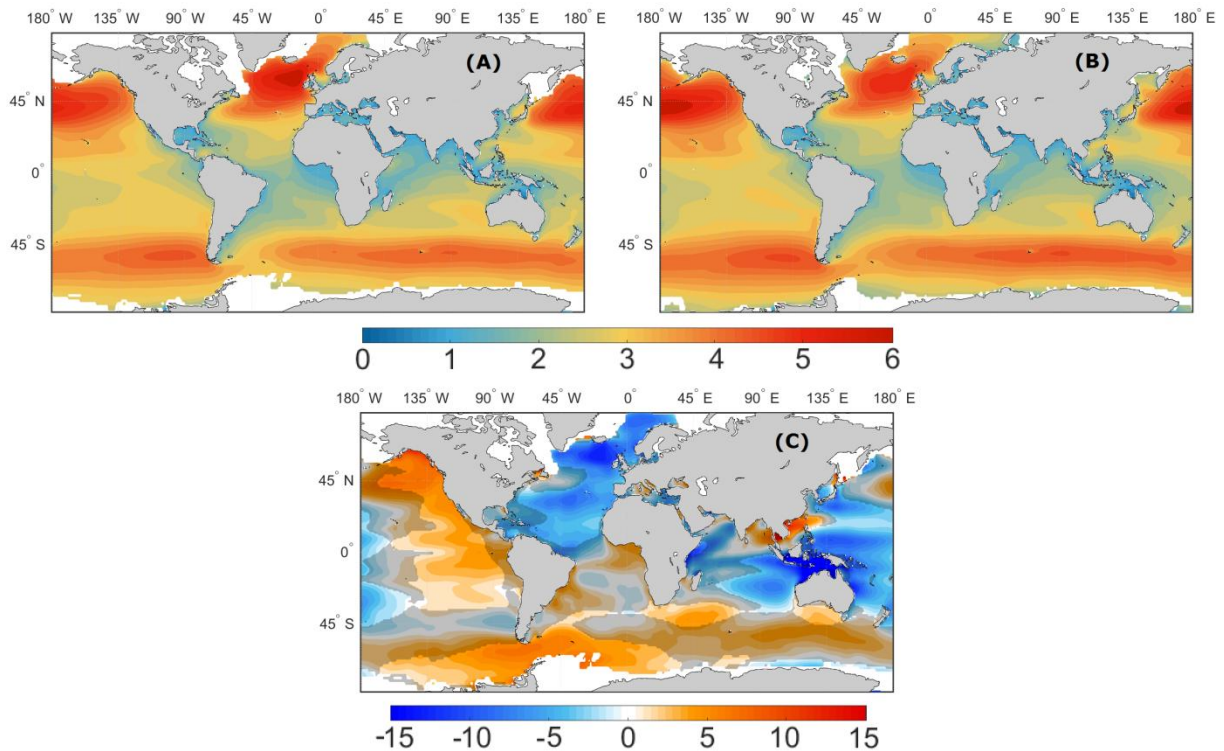


*Figure 10 – As in Fig. 9, but for DJF.*

Fig. 11 displays the JJA PC20 and FC21 $H_S$ means, as well as the corresponding normalized difference between future and present climates. A nearly 15% statistically significant positive difference along the Indian sector of the Southern Ocean and south of Australia is expected for the austral winter (Fig. 11c). The Southeastern Pacific Ocean also reveals are large area of statistically significant expected increases in wave height, mostly between 5% and 10%. The considerable projected decreases previously shown for Indonesia and all its surroundings in DJF (in Fig. 10c) are now (in JJA; Fig. 11c) mainly positive, although non-statistically significant.

Another interesting (despite non-statistically significant) feature is also observed in JJA, along the west coast of the Iberian Peninsula: a future projected increase in $H_S$ along the Southeastern flank of the North Atlantic Gyre (Fig. 11c), most likely arising from an equivalent expected boost in wind speeds in that area (Fig. 12f), that can be explained assuming a poleward expansion of the Hadley cell (and a respective poleward displacement of the northeasterly trade winds) in a future global warming scenario (Kang and Lu, 2012; Semedo *et al.*, 2015).
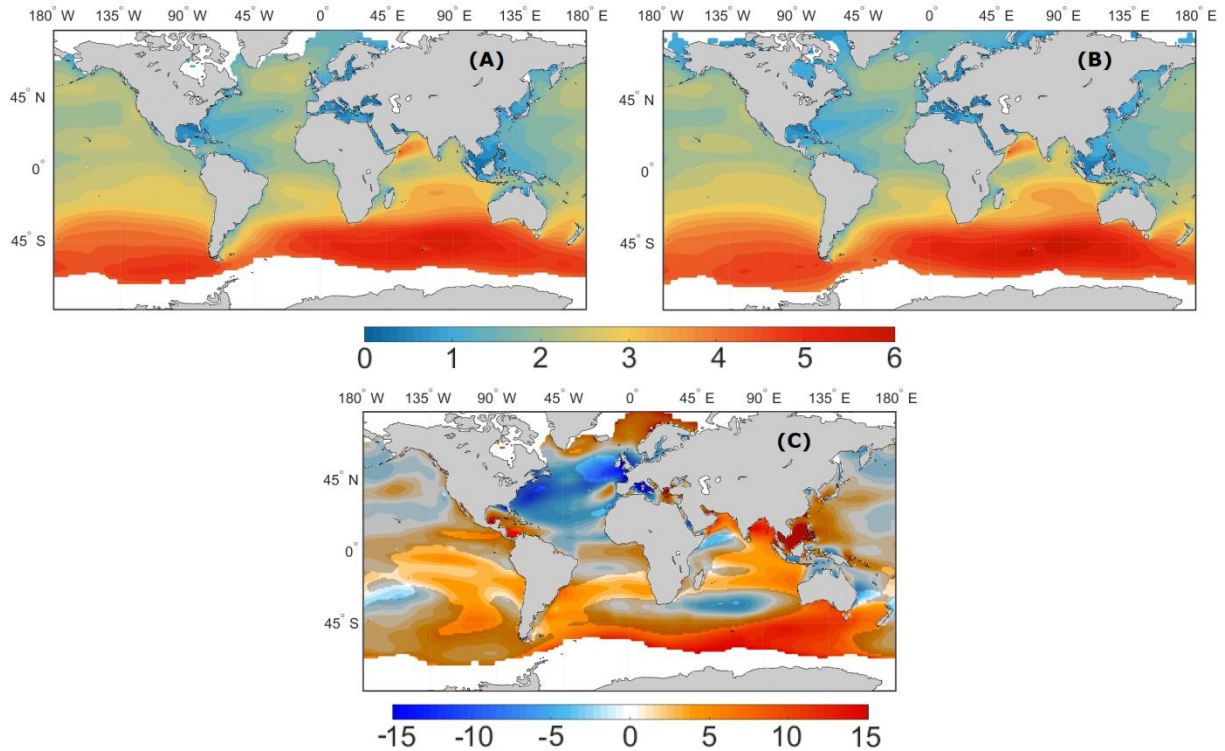
*Figure 11 – As in Fig. 9, but for JJA.*

All considered, wave height increases can be expected for the 2071-2100 period, due to climate change as reproduced by the RCP8.5 scenario. These increases are more relevant in the Southern Hemisphere, particularly during JJA (global mean differences of +1.07%, -0.69% and +2.60% for the annual, DJF and JJA time intervals, respectively, being the mean normalized differences positive in 64.82%, 53.42% and 73.93% of the globe in the same periods). The $H_S$ projected increases in the Southern Ocean, as seen in Figs. 9-11, can also have an impact on the global mean wave periods ($T_m$), due to higher wave heights at the generation areas, and a longer propagation distance towards the equator (considering the retraction of the sea ice cover extent). Climatic change of the $T_m$ field is analyzed in the next subsection.

Fig. 12 presents the PC20 annual, DJF and JJA global $U_{10}$ means, and the correspondent (normalized: FC21 minus PC20 normalized by PC20) projected differences for the end on the twenty-first century. Present climate maps display the highest $U_{10}$ mean values over the mid-to-high latitudes of each hemisphere, associated with the extratropical storm tracks. Seasonally, the corresponding winter hemisphere shows highest near surface wind speeds. The trade winds are also easily noticeable, especially in the DJF and JJA maps (Figs. 12c,e). At the first glance the $H_S$ (Figs. 10a, 11a, and 12a) global patterns seem similar to the corresponding $U_{10}$ field (Figs. 12a,c,e). A more detailed analysis leads to the conclusion that

34

the waves and the overlaying winds are somewhat detached, due to the wave propagation effect. This detachment is lower in the extratropical latitudes (particularly in the corresponding winter), and much higher in the intertropical latitudes, being highest in the "swell pools". For this reason, due to the referred propagating effect of the waves, the connection between the projected changes in the wind speed and the changes in the ocean surface waves is not local: for example, changes in terms of wind speed and direction in the extratropical storms will affect the wave climate in the low latitudes, without the need of any considerable changes in the wind climate there.
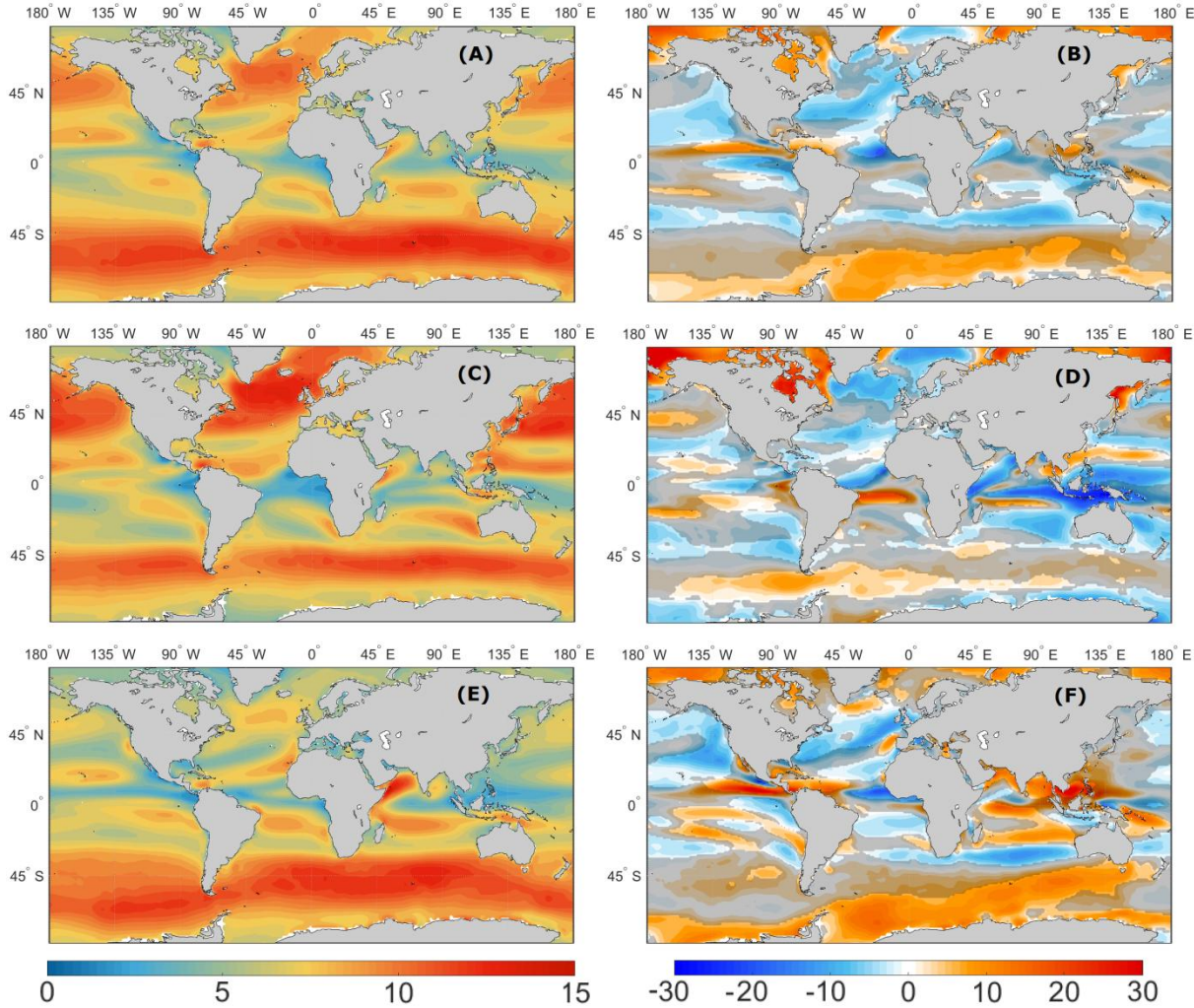


*Figure 12 – (A) Annual, (C) DJF and (E) JJA means of $U_{10}$ (m/s), for PC20, and (B, D, F) respective $U_{10}$ normalized differences (%): FC21 minus PC20 normalized by PC20.*

The projected future changes of $U_{10}$ (Figs. 12b,d,f) exhibit statistically significant annual and seasonal (DJF and JJA) decreases along the subtropics and midlatitudes of the Northern Hemisphere. In the high latitudes and polar areas, statistically significant increases can be found, mainly due to the creation of ice free zones in the open ocean. These are more

prominent during DJF in the Arctic Ocean, and in JJA in the Southern Ocean (also due to the intensification of local storms). Positive differences are also present in the ITCZ (Intertropical Convergence Zone): its seasonal displacement is easily observable.

## 4.2    Mean wave period ($T_m$)

The $T_m$ annual means of PC20 and FC21, along with its normalized differences, are shown in Fig. 13. The highest wave periods are present over the eastern parts of the three major basins (Pacific, Atlantic and Indian oceans), especially in the Southern Hemisphere and tropical regions. As waves propagate away from their generation area as swell, their height decreases and their period increases, therefore, the climatological maxima of $T_m$ and $H_S$ do not coincide. Wave periods are higher along the previously mentioned "swell pools", in the low and tropical latitudes, where waves are smaller but longer.

The normalized differences between present and future climates (FC21 minus PC20 normalized by PC20; Fig. 13c) exhibit large areas of statistically significant projected increases in $T_m$ (up to 10%; 1-2 s) prevailing mostly below the equator line, and along the west coasts of the American, African and Australian continents. Nevertheless, positive differences are also present in the high latitudes of the Northern Hemisphere (east of Greenland and north of Norway, in the Barents Sea), due to sea ice retraction, as mentioned before regarding the significant wave height projections. Statistically significant decreases in wave periods are expected only northeast of Papua New Guinea, and in the North Atlantic Ocean, around the Iberian Peninsula and west of the British Isles, all less than 5% (~1 s).
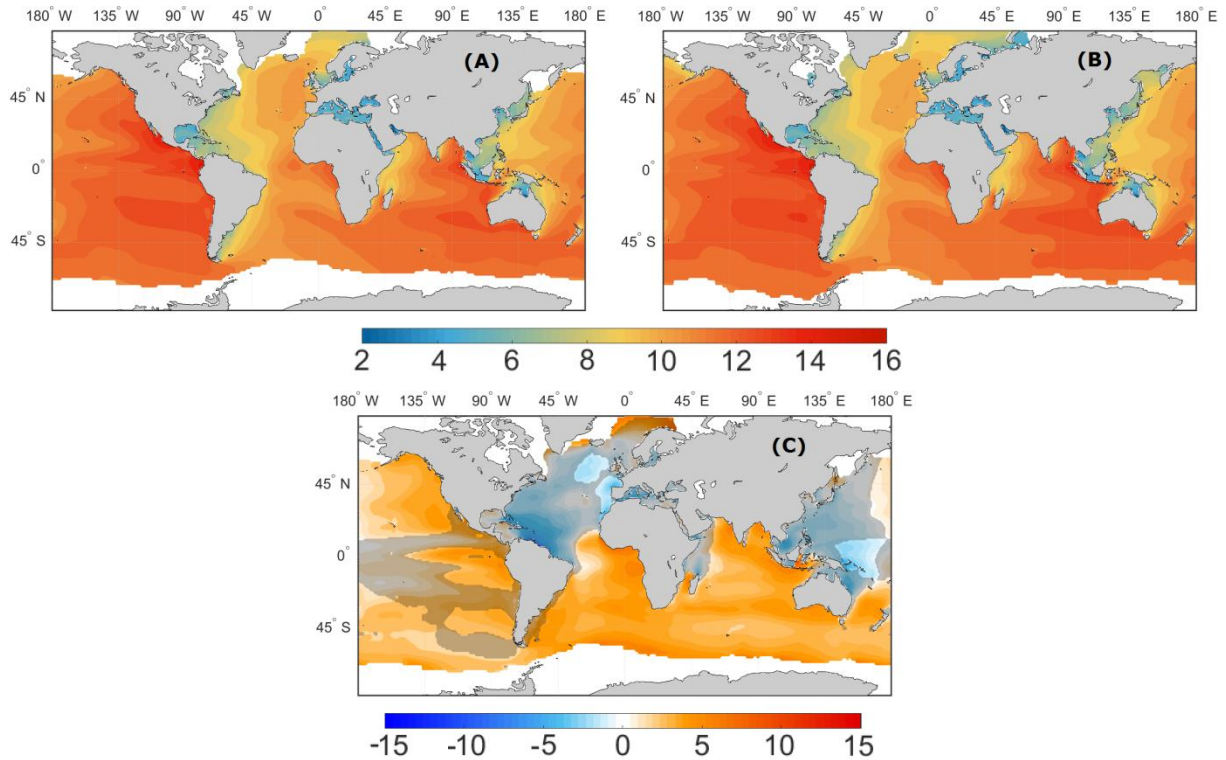
*Figure 13 – Annual means of $T_m$ (s), for (A) PC20 and (B) FC21, and (C) $T_m$ normalized differences (%): FC21 minus PC20 normalized by PC20.*

The DJF PC20 and FC21 $T_m$ means, and the corresponding normalized differences between future and present climates are shown in Fig. 14. During the boreal winter, statistically significant projected decreases in $T_m$ expand all across the North Atlantic and West Pacific oceans (up to 5%), as it can be seen in Fig. 14c. In the Southern Hemisphere, a slight increase is still projected, mainly between 2% and 3% (less than 1s), but locally reaching 5% along the equatorial regions of the Eastern Pacific and Indian oceans.
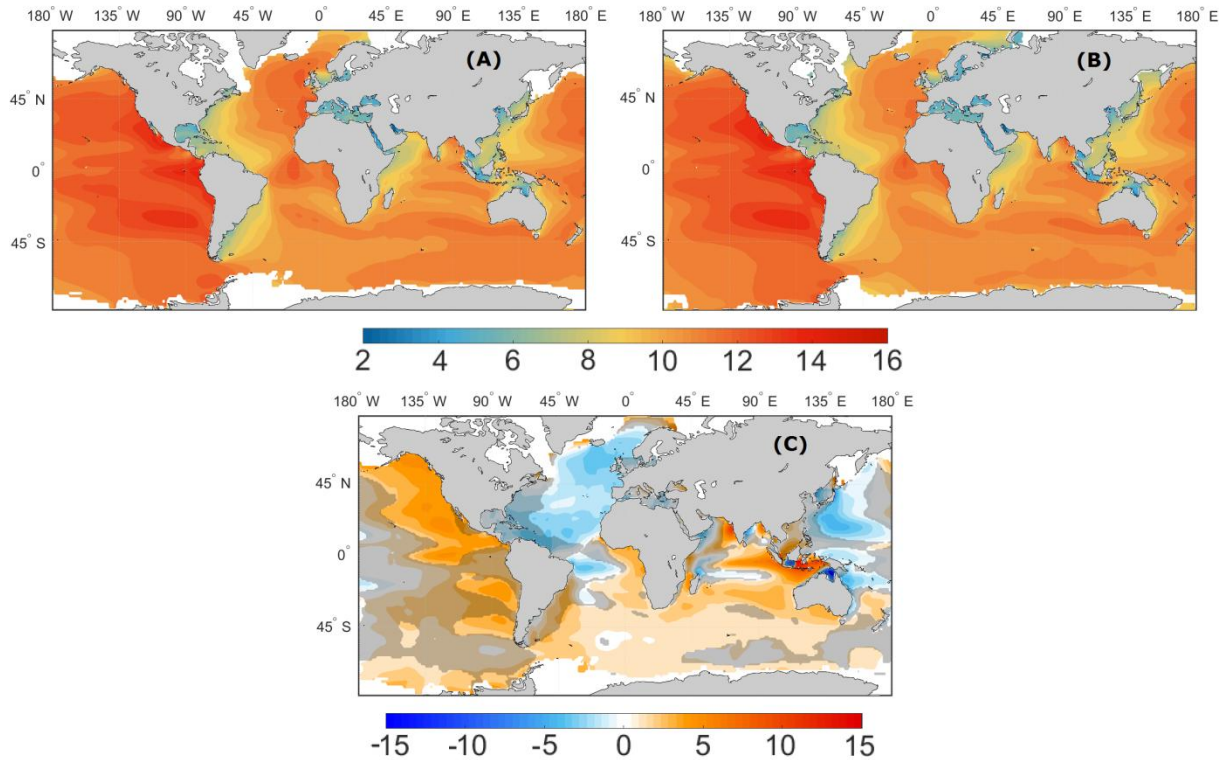
*Figure 14 – As in Fig. 13, but for DJF.*

During the boreal summer (JJA; whose PC20 and FC21 means, and normalized differences between them, are shown in Fig. 15), excluding a very narrow area east of the Indonesian archipelago, all the statistically significant projected changes are positive, the highest between 5% and 10% (1-2 s) in the Southern Ocean, tropical regions of the Atlantic Ocean and along the west coast of the United States of America (Fig. 15c). Assuming the northwards swell propagation from the Southern Ocean, the aforementioned (in the previous subsection) projected increase in $H_S$ over that area in JJA might be connected to the global wide expected increase in $T_m$ in the same period.
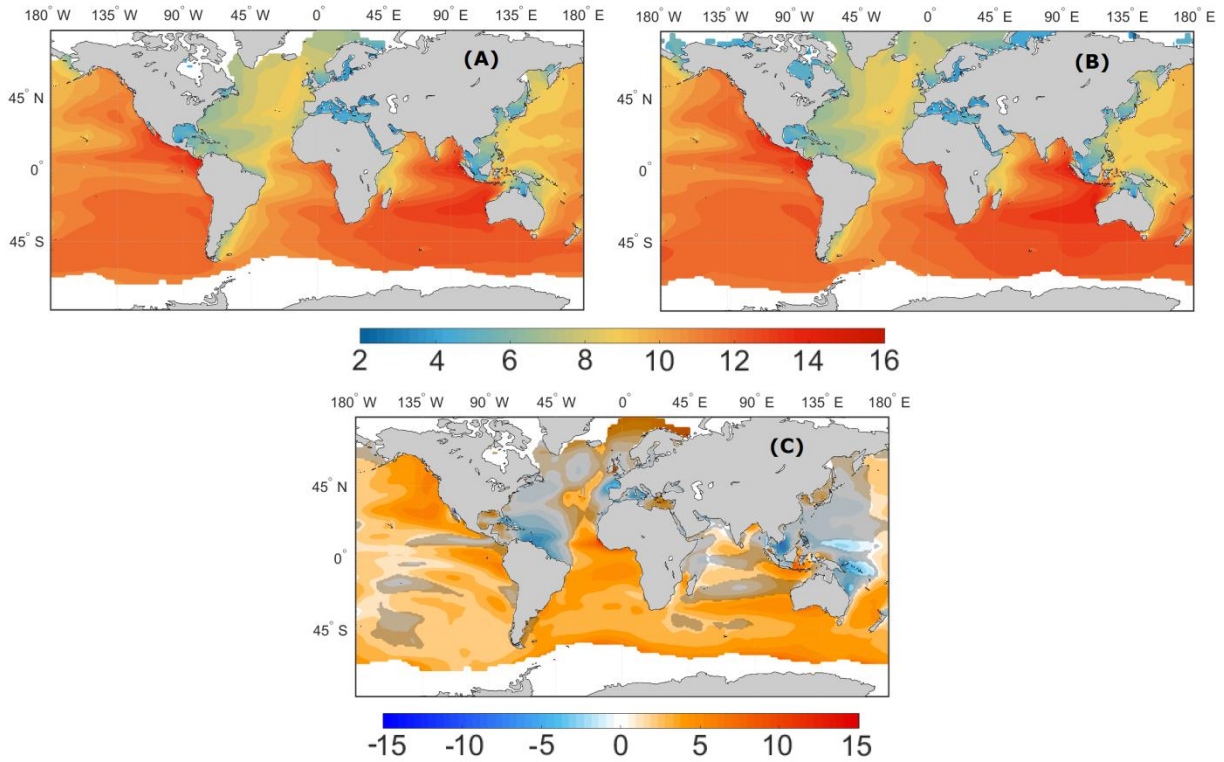
*Figure 15 – As in Fig. 13, but for JJA.*

Altogether, $T_m$ statistically significant increases for the period 2071-2100 can be expected, especially during the austral winter (Fig. 15c), and along the Southern Ocean and Eastern Pacific and Indian oceans, as well as in the South Atlantic Ocean. Global mean differences of +1.39%, +0.52% and +2.10% for the annual, DJF and JJA time intervals are found, respectively, being the mean normalized differences positive in 79.99%, 71.14% and 87.48% of the globe in the same periods. Slight decreases are projected for the North Atlantic Ocean and South coast of Japan, in DJF (Fig. 14c).

### 4.3    **Mean wave direction (MWD)**

Shoreline position is equally sensitive to directional changes as to changes in wave height (Coelho *et al.*, 2009). An analysis of the impact of climate change in future mean wave front direction is presented in this subsection. The mean annual MWD for PC20 and FC21 are displayed in Fig. 16, as well as the anomalies between future and present MWD climates (FC21 minus PC20), with the overlaying arrows representing the mean values for both time-slices. The widespread westerlies influence over the Southern Ocean is undoubtedly present, and the wave propagation tracks resulting from the effect of the trade winds on the ocean surface are also noticeable along the tropical and subtropical latitudes. In the Southern

Hemisphere mean wave directions transit from a strong westerly component (~270º) in the mid-to-high latitudes, to a southerly propagation (~180º) in the subtropical latitudes, and eventually gaining an easterly component near the equator. In the Northern Hemisphere, this transition is also observed, but this time, as the latitude decreases, the main westerly propagation turns to a northerly propagation (~0º). These mean wave propagation patterns are visibly similar to the major ocean gyres.

Positive (clockwise) anomalies can be observed mainly in the tropical and subtropical regions of both hemispheres, associated with more easterly and southerly projected wind waves in the northern and southern portions, respectively, being these features consistent with a larger contribution of Southern Ocean swell (Hemer *et al.*, 2013a). Negative (anticlockwise) anomalies occur mostly along the mid-to-high latitudes of both hemispheres (westerly regions), corresponding to an increased southerly component associated to the shifting of the storm tracks to higher latitudes (Arblaster *et al.*, 2011), considering the polar sea ice retraction.
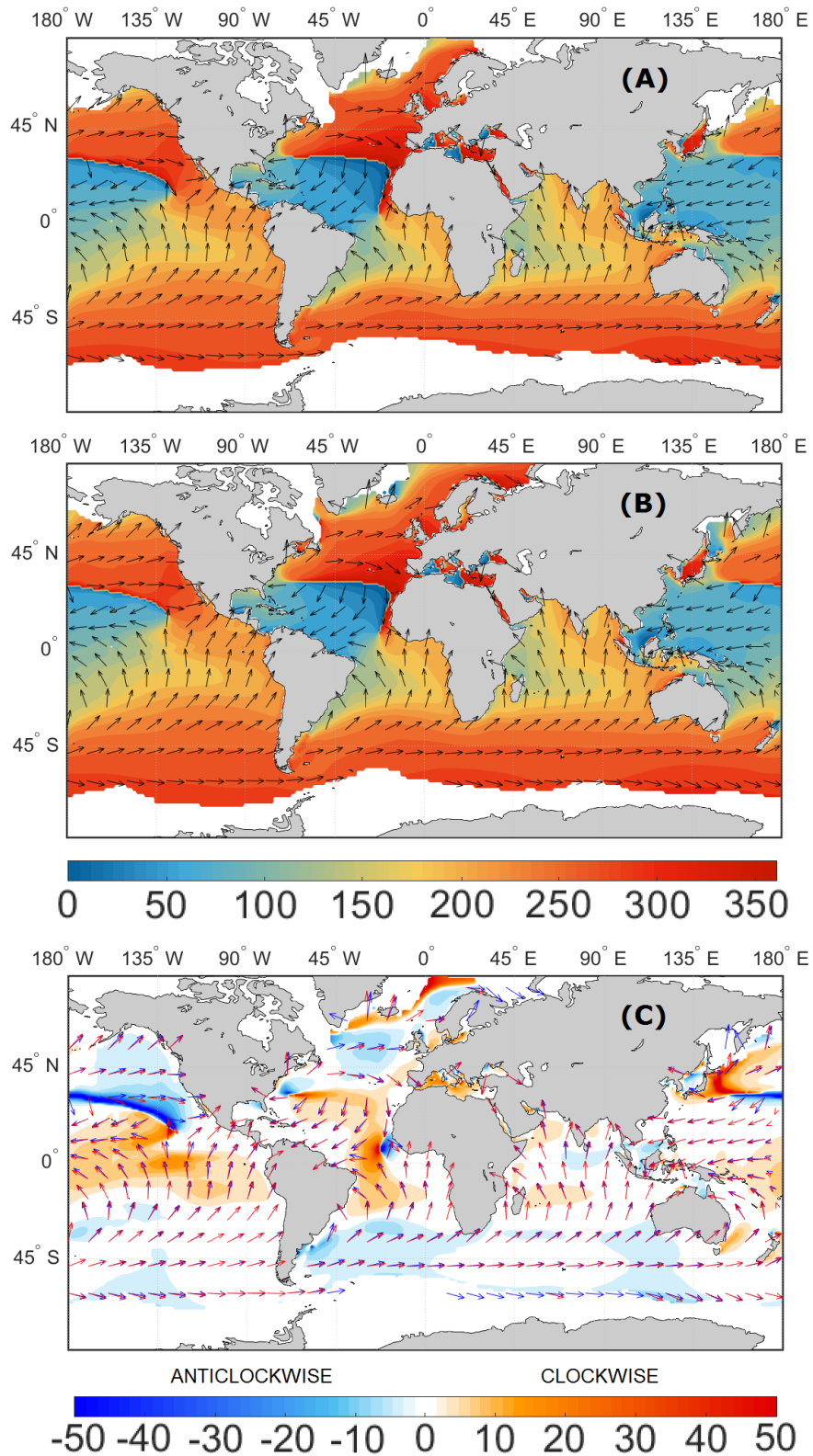
*Figure 16 – Annual means of MWD (º), for (A) PC20 and (B) FC21, and (C) MWD anomalies (º): FC21 minus PC20.*

Seasonally, the main differences are found over the tropical and subtropical regions of the summer hemisphere. The DJF PC20 and FC21 MWD means, and the corresponding anomalies between future and present climates are shown in Fig. 17. During this season, in the Northern Hemisphere, a stronger westerly propagation is visible along the extratropical regions (storm tracks). As the ITCZ lowers in latitude, a more northerly component is present in the tropical and subtropical latitudes, especially in the Central Pacific Ocean, where the northerly propagation (mainly as swell) reach 30ºS. Clockwise rotations are expected for the southern equatorial regions of the three major ocean basins (Fig. 17c), associated with an increased southerly component in the Atlantic and Indian oceans, a more southwesterly flux in the west coast of South America, and an intensified north-to-northeasterly propagation in the North and Eastern parts of the Pacific Ocean. Anticlockwise rotations are projected to occur in the mid-to-high latitudes of both hemispheres, referring to a more westerly propagation in the Southern Ocean, and an intensified west-to-southwesterly propagation in the North Atlantic Ocean.

The JJA PC20 and FC21 MWD means, and the corresponding anomalies between future and present climates are shown in Fig. 18. During this season a stronger propagation from West (~ 270º) is observed in the Southern Ocean. An intensified southerly flux (associated with swell propagation from the Southern Ocean) is visible in the Pacific and Indian oceans, but also in the South Atlantic Ocean. The prevailing anomalies are present in the Northern Hemisphere. The projected clockwise rotation almost in the entire Pacific Ocean to a more southerly mean direction reveals the previously mentioned intensification of the Southern Ocean swell contribution. In the North Atlantic Ocean, the anomaly pattern suggests a slight poleward shift of its main oceanic gyre.
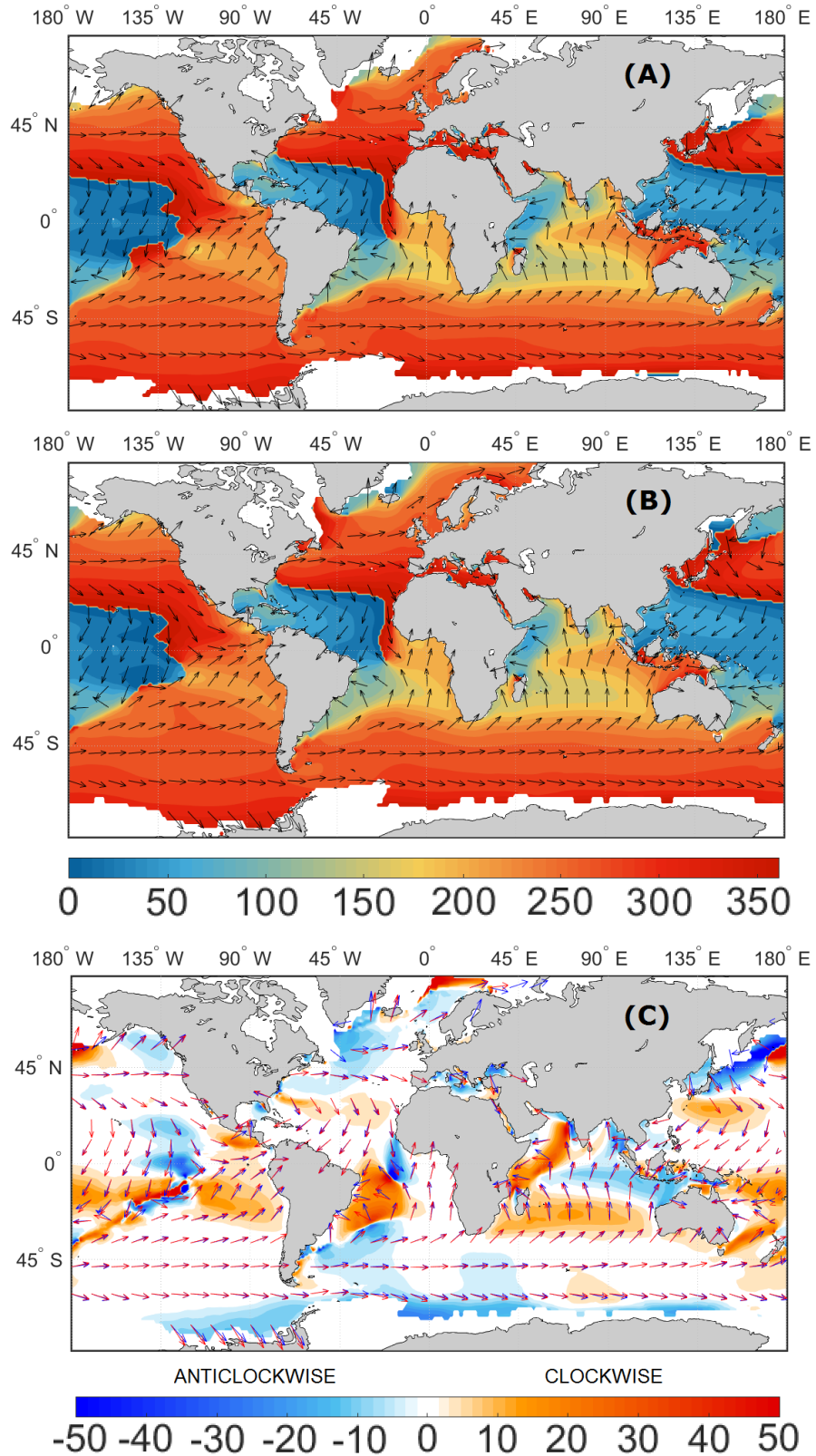
*Figure 17 – As in Fig. 16, but for DJF.*
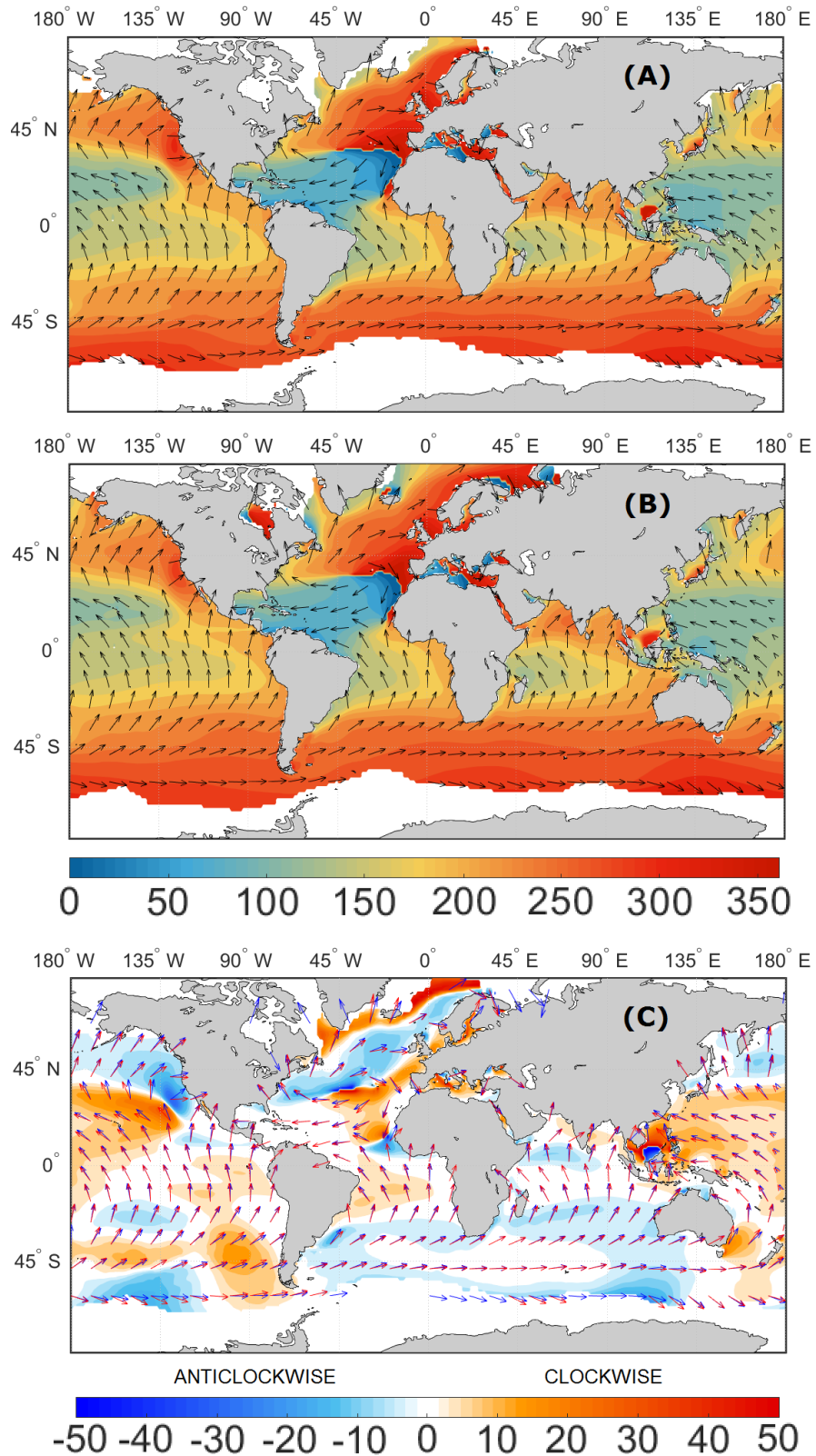
*Figure 18 – As in Fig. 16, but for JJA.*

## 4.4    Wave energy flux (power, $P_w$)

Wave power is a function of the distribution of wave periods and heights, to the first and second orders, respectively ($P_w = (\rho g^2/32\pi)\, T_m H_S{}^2$, as in Young, 1999). Hence, it is only natural for its projected future patterns to be dominated by changes in $H_S$, as in annual and seasonal means, as in the respective normalized differences (FC21 minus PC20 normalized by PC20). Yet, absolute values differ a lot from the $H_S$ ones, as it will be observable in further Figs. 19a,b, 20a,b and 21a,b.

The PC20 and FC21 annual $P_w$ means, along with the corresponding normalized differences are exhibited in Fig. 19. The annual highest statistically significant normalized projected differences present in Fig. 19c are located along the Southern Ocean, near Antarctica, reaching almost 30% (~40 W/m locally; the Southern Hemisphere uniquely shows statistically significant projected wave power increases, except from a very small area Northeast of New Zealand). Statistically significant $P_w$ increases are also present in the Southeastern Pacific Ocean (up to 10%) and in the high latitudes of the Northern Hemisphere (e.g. Gulf of Alaska and Arctic sea) due to the expected sea ice retraction. The North Atlantic Ocean detains the only region with statistically significant projected decreases, up to 15% (15 W/m), south of Iceland and southwest of the Azores archipelago.
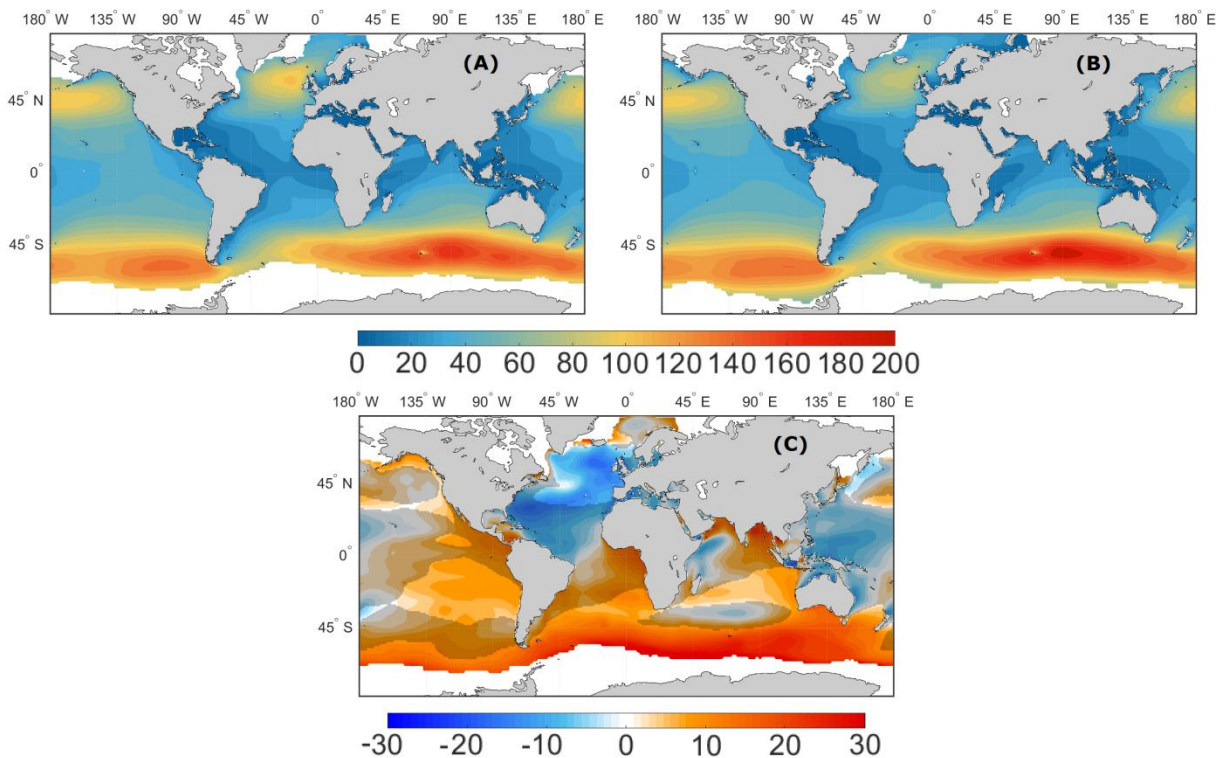


*Figure 19 – Annual means of $P_w$ (W/m), for (A) PC20 and (B) FC21, and (C) $P_w$ normalized differences (%): FC21 minus PC20 normalized by PC20.*

45

The DJF PC20 and FC21 $P_w$ means, and the corresponding normalized differences are shown in Fig. 20. During this season, the maximum mean values are present in the mid-to-high latitudes of the Northern Hemisphere, resulting from the highest storm activity along the extratropical regions. Present climate (PC20) mean wave power values reach 180 W/m south of Iceland. It is also in this location that the nearly 15% decrease in $H_S$ is expected, resulting in an almost 30% (~50 W/m) projected decrease in $P_w$ in the same area, assuming slight variations in $T_m$, as seen in section 4.2. Considerable decreases are also to be expected in Indonesia and its surroundings (Indian Ocean and West Pacific Ocean; Fig. 20c). Up to 10% projected increases in $H_S$ in the East Pacific Ocean (especially in the midlatitudes of the Northern Hemisphere) will support local 20% positive statistically significant differences in wave power. In the Southern Ocean, mainly between the Ross and Weddell seas, statistically significant increases in $P_w$ are also visible, peaking at 15% (~12 W/m) along the Drake Passage.
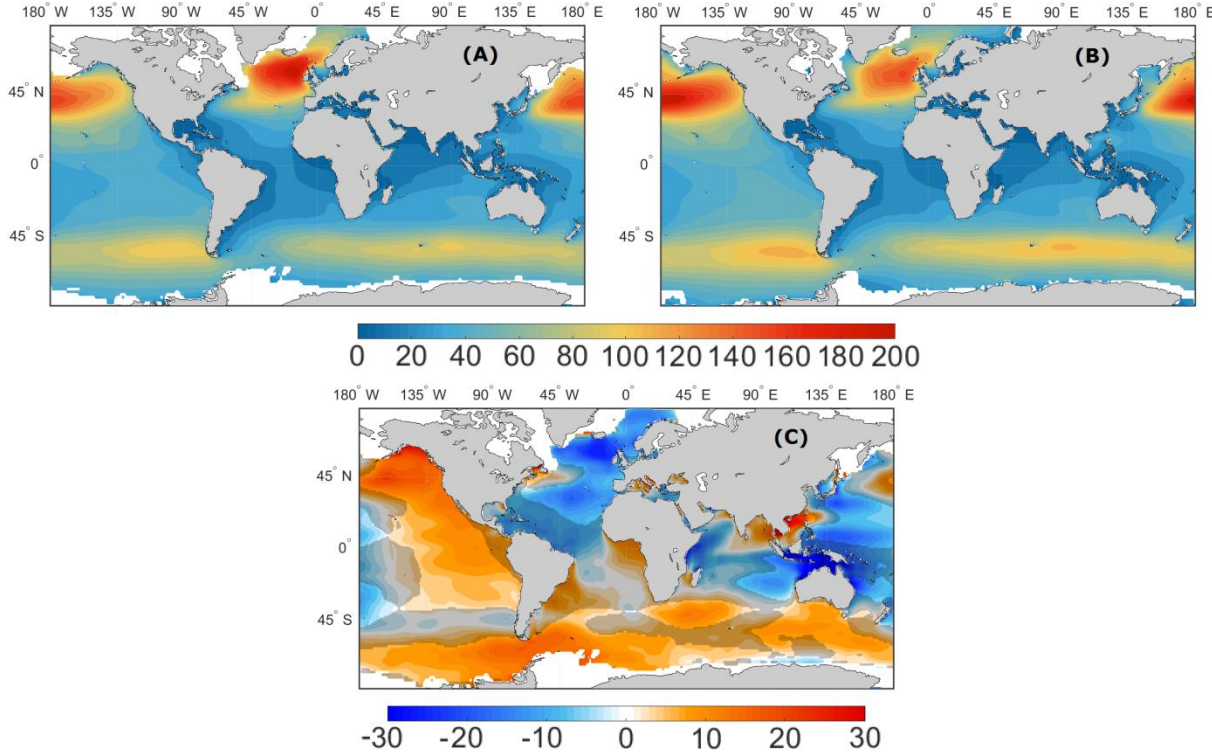


*Figure 20 – As in Fig. 19, but for DJF.*

The JJA PC20 and FC21 $P_w$ means, and the corresponding normalized differences are shown in Fig. 21. During this season, the South Hemisphere dominates the projections, as in mean values, as in statistically significant differences. Mean energy fluxes over 100 W/m are only present along the austral storm belt and statistically significant expected increases are visible in the Southern Ocean (reaching 30%, approximately 40 W/m Southwest of Australia),

46

and in the Southeastern portions of the Pacific, Atlantic and Indian basins (10% to 15%). Positive differences (although statistically non-significant) are present in the Northeastern Pacific Ocean and north of Indonesia, along the Gulf of Thailand and South China Sea. The only projected decreases in $P_w$ for this season take place in the North Atlantic Ocean, northeast of Australia, some areas of the Indian Ocean, and east of New Zealand, in the South Central Pacific Ocean, being all statistically non-significant, except for a reduced area Northeast of New Zealand.
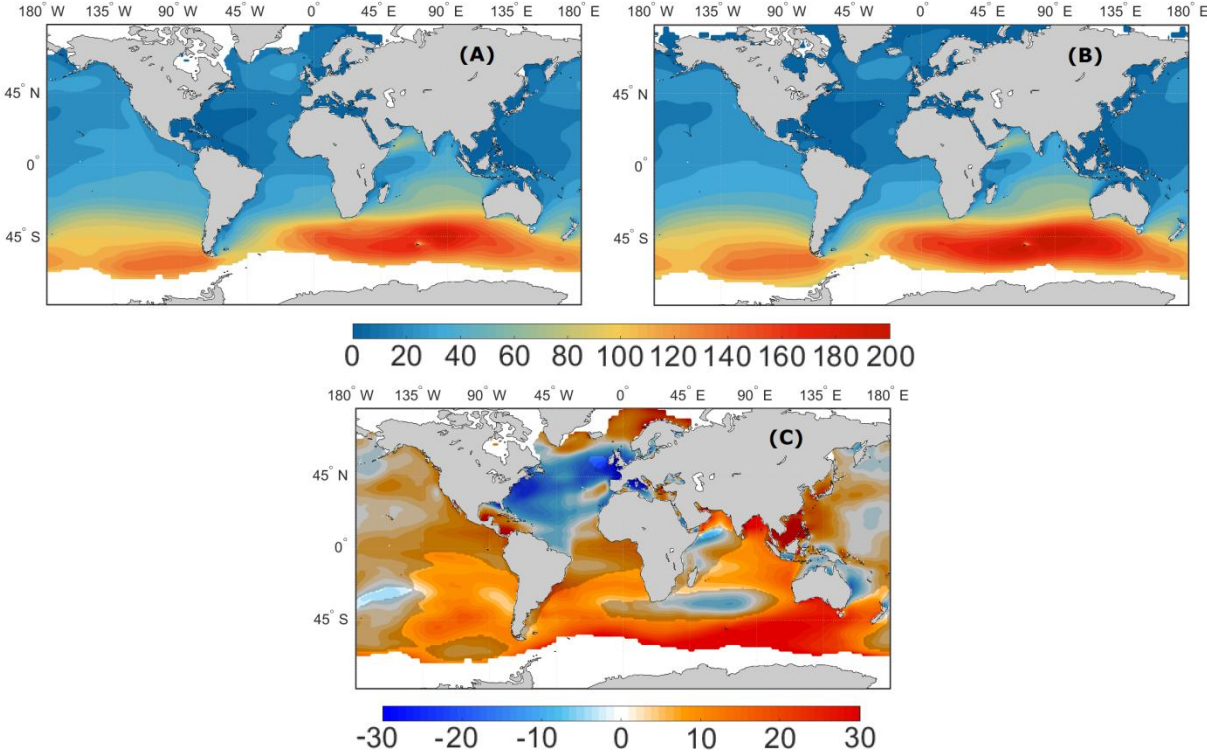


*Figure 21 – As in Fig. 19, but for JJA.*

Altogether, projections show statistically significant wave power projected increases at a global scale for the 2071-2100 period, excluding the North Atlantic Ocean, the west half of the Pacific Ocean and the Indonesian archipelago in DJF. Global mean differences of +3.90%, +0.07% and +7.18% for the annual, DJF and JJA time intervals are found, respectively, being the normalized differences positive in 70.70%, 58.47% and 81.43% of the globe in the same periods.

# 5. EOF analysis

Wave fields interannual variability patterns were obtained by performing an empirical orthogonal function (EOF) analysis (von Storch and Zwiers, 1999) to the PC20 and FC21 $H_S$ and $P_w$ detrended annual and seasonal (DJF and JJA) mean fields, over the North Atlantic Ocean sub-basin. This region, as mentioned before, is projected to be exposed to a significant decrease in wave heights and mean wave periods (and hence to a wave energy flux), especially during DJF, differing from the main global projected wave climate behavior, where wave heights are, in general, expected to increase. The window of analysis was set to cover latitudes from 0º–75ºN and latitudes from 100ºW–20ºE. The Mediterranean and Baltic Seas data was ignored (masked) in the EOF analysis, in order to avoid contamination of the results.

The EOF is the method of choice for analyzing the variability of a single field (of only one scalar variable). It finds the spatial patterns of variability, their time variation, and gives a measure of the "importance" of each pattern. The EOF method breaks the data into "modes of variability", but these modes are primarily *data modes* and not necessarily *physical modes*. Whether they are physical is a matter of careful subjective interpretation (Björnsson and Venegas, 1997). The "classic" method to perform an EOF is by computing the eigenvectors of the temporal covariance matrix of each data set. If the eigenvectors are put in order according to the size of the eigenvalues, then the first EOF is the eigenvector associated with the highest eigenvalue. The one associated with the second highest eigenvalue is the second EOF, and so on. To access some of the limitations of the "classical" EOF analysis, these can be rotated ("rotating" the eigenvectors), so that the resulting patterns are more physically interpretable. If the modes are not to be physically interpreted, but to be used for other purposes (prediction, pattern recognition, noise reduction, etc.) rotation is probably not necessary (Björnsson and Venegas, 1997). Only the first rotated EOF (EOF1) is shown in this subsection.

Fig. 22 depicts the annual and seasonal (DJF and JJA) PC20 $H_S$ and $P_w$ EOF1 spatial patterns. For both fields, the spatial patterns of the leading modes are qualitatively comparable to each other. Explained variances of these patterns at the annual scale (Figs. 22a,d) are of 41.10% for $H_S$ and 38.10% for $P_w$. Their structure displays dominating anomalies of one sign (maxima of the explained variances in the mid-to-high latitudes) and slight magnitude anomalies of the opposite sign the lower latitudes. $H_S$ anomalies are spatially less pronounced than the $P_w$ ones, mainly on an annual scale, showing a lower wave height gradient along the sub-basin, which leads to conclude that the $H_S$ field is more homogeneous

when compared to the wave power field, as it was expected, since $P_w$ is a function of $H_S$ to the second order, having a larger range of values than the wave height field, leading to higher geographical gradients.

An extended arm of slightly positive anomalies along the eastern half of the sub-basin, more prominent in $H_S$ (almost reaching the Equator line) but also visible in $P_w$ (reaching the Canary Islands), is present in DJF (Figs. 22b,e). These patterns are associated to the winter south-eastward propagating swell, away from the main wave generation areas south of Iceland, and mainly during this period of maximum activity along the North Atlantic extratropical storm belt (winter in the Northern Hemisphere). For this reason, this arrangement is not widely observable in JJA (Figs. 22c,f). There is, nevertheless, a thin extension of the positive anomalies in the $H_S$ field during the summer (in the Northern Hemisphere), but these may be attributed to the strong northerly winds (and consequently a more robust wave height field) alongside the western coast of the Iberian Peninsula in JJA (as seen in Fig. 12e).

The main differences between DJF and JJA, shown in Figs. 22b,c (DJF) and 22e,f (JJA), lie on the latitude of the maximum explained variances (main centers of action): during JJA, a positive latitudinal shifting is visible for the $H_S$ and $P_w$ fields (more notably in terms of wave heights) due to the shift of the mean storm tracks to higher latitudes during the summer. The seasonal explained variances for the observed patterns are of 23.40% and 19.85% for wave height and 30.00% and 25.20% for wave power, in DJF and JJA respectively. The lower explained variances found for the local summer are connected to the lower intensity and pattern definition (lower gradient) of the analyzed wave fields during this period.

The first EOF (EOF1) of the projected spatial patterns of annual and seasonal (DJF and JJA) FC21 $H_S$ and $P_w$ are displayed in Fig. 23. This analysis is analogous to the PC20 one, with similar results, with an identical behavior in all the panels. The explained variances of these future projected patterns are of 39.20% and 33.45% for $H_S$ and $P_w$ at an annual scale, 21.65% and 25.25% for DJF, and 20.90% and 25.75% for JJA, respectively. In spite of the similarity of the results between present and future projected climates, subtle changes in their intensity and spatial distribution can be observed. These are addressed in Fig. 24, that shows the juxtaposition between the maps of the present and projected future climate (PC20 and FC21) EOF1 patterns, with background faded colors from the PC20 EOF1 analysis, which facilitates the interpretation of their differences. In terms of $H_S$, the FC21 projected annual

pattern of anomalies differs from the PC20 one mostly in the mid-to-high latitudes (~45ºN–60ºN), where its absolute values tend to be lower. Seasonally, lower wave height projected positive anomalies are also found for the referred area. During DJF, the aforementioned winter pattern of swell propagation across the eastern half of the North Atlantic sub-basin, easily observable in Figs. 22b and 23b, is enhanced in future projections, reaching the Gulf of Mexico. Still during DJF, the main wave height center of action is projected to negatively shift in latitude (~3º; Fig. 24b). In JJA (Fig. 24c), this shift is slightly positive (~2º). Wave energy flux ($P_w$) future projected EOF1 (Figs. 24d,e,f) shows smoother discrepancies compared to the present climate (PC20), with an extremely similar annual expected anomaly pattern, although less intense (lower gradient). On a seasonal scale (DJF and JJA; Figs. 24e,f), not only the maximum anomalies in the ~45ºN–60ºN region tend to be higher (slightly stronger field), but a lightly-positive latitudinal shift of these centers of action is also noticeable (~2º).

Altogether, projections show a general reduction of intensity in the wave height and wave power centers of action (excluding $P_w$ in DJF and JJA), by the end of the twenty-first century (projected reduced variability), in the North Atlantic sub-basin. These results are in line with the referred expected decrease in the magnitude of wave height and power in that area (Figs. 9c, 10c, 11c, 19c, 20c, and 21c), along with a decrease in their spatial gradient, supported by the lower explained variances for the mean patterns of the projected $H_S$ and $P_w$ fields (again, excluding $P_w$ in DJF and JJA).

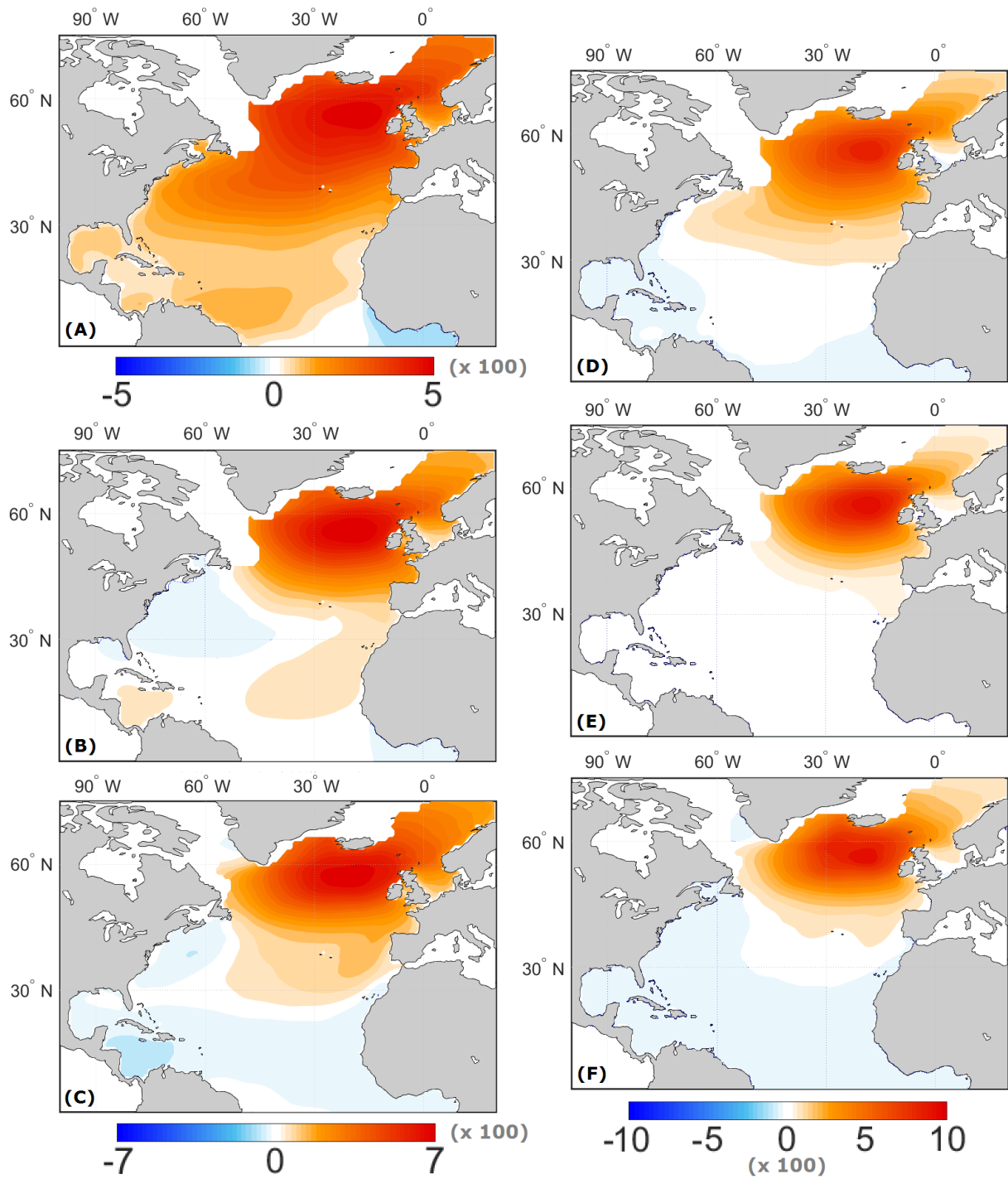*Figure 22 – First EOFs fields of PC20 $H_S$ (A) annual, (B) DJF and (C) JJA, and $P_w$ (D) annual, (E) DJF and (F) JJA. The color scales vary between the panels.*
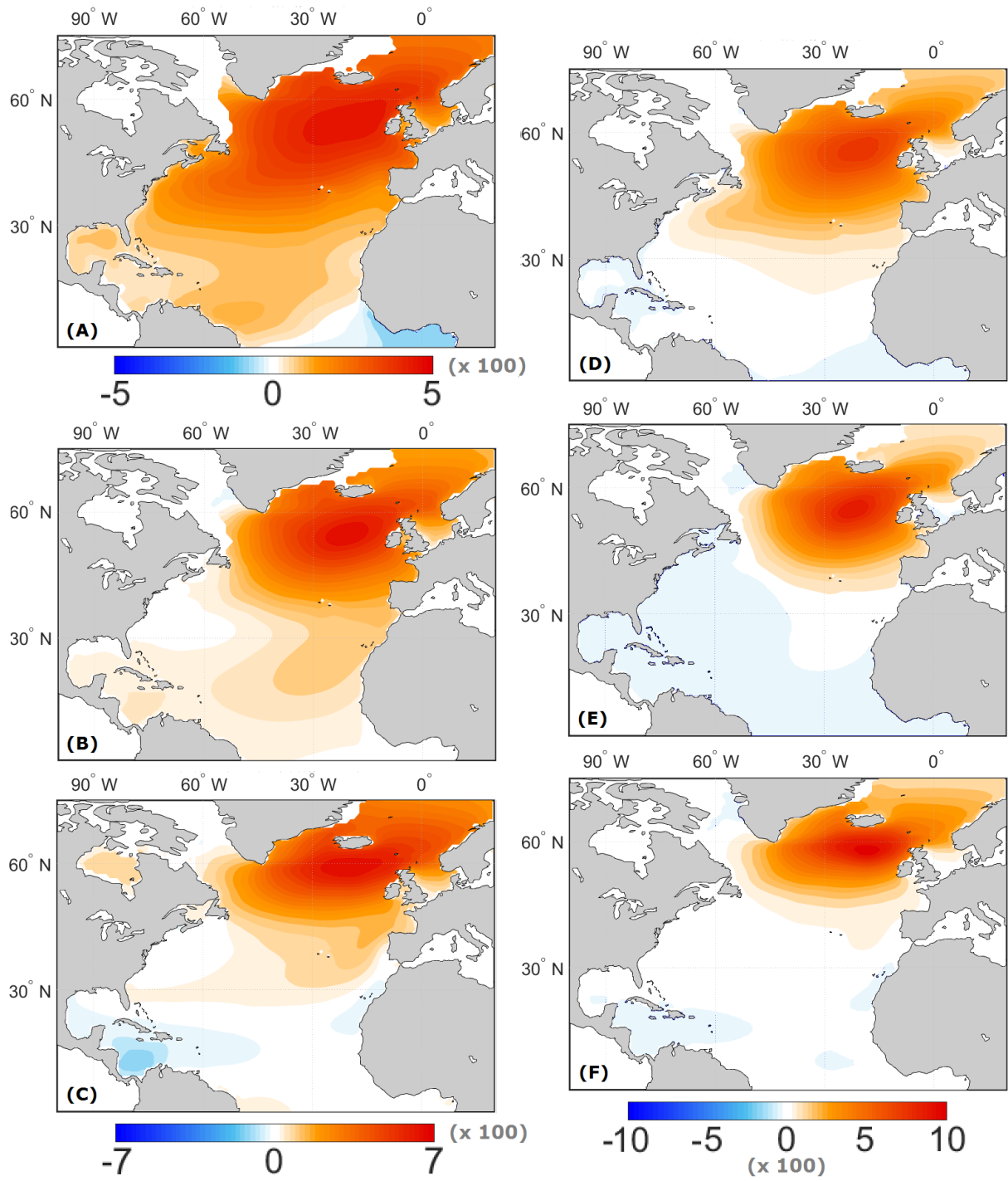
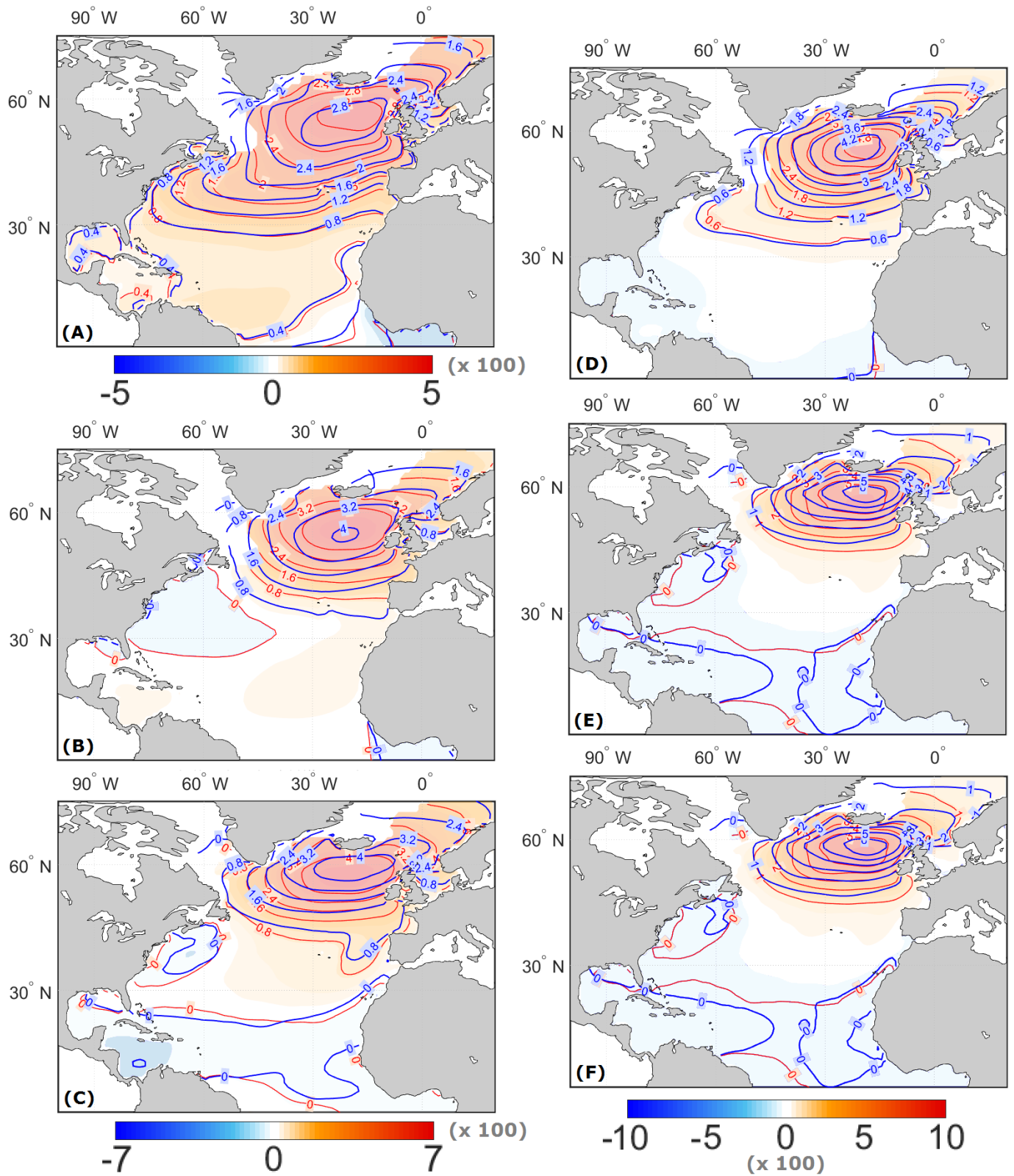*Figure 23 – As in Fig. 22, but for FC21.*

*Figure 24 – Juxtaposition between the first EOFs fields of PC20 (red lines; faded background colors) and FC21 (blue lines) $H_S$ (A) annual, (B) DJF and (C) JJA, and $P_w$ (D) annual, (E) DJF and (F) JJA.*

# 6.    Discussion

Global warming, as a form of climate change, will affect the global wave climate by the end of the twenty-first century (IPCC, 2013). The previous sections (4 and 5) showed that wave heights ($H_S$) are projected to increase mainly in the Southern Ocean (where a moderate increase in wind speed ($U_{10}$) is also projected to occur) and decrease considerably in the North Atlantic sub-basin, along with a projected decrease in its centers of action's intensity (less variability). These results are in line with the expected changes in the global wave height climate from CMIP3 (e.g. Hemer *et al.*, 2013a), and particularly CMIP5 (e.g. Dobrynin *et al.*, 2012) simulations, although there are some slight changes, for instance, a more pronounced projected decrease in the global annual mean wave height when compared to the CMIP3 ensemble of wave-climate projections (35.18% *vs* 25.80%), and higher values of mean annual $H_S$ along the Southern Ocean when compared to the CMIP5 study. The wave energy flux field ($P_w$) projected changes show a similar behavior to the $H_S$ ones, although, there is an intensification and slight poleward shift of its centers of action is visible both in DJF and JJA.

Another way of objectively analyze the absolute and spatial changes of the $H_S$ and $P_w$ wave fields between present climate and the future projected climates is through the interpretation of North-South cross sections of the zonally averaged annual and seasonal means of the respective parameters, present in this section, for three different ocean basins: Atlantic Ocean, Pacific Ocean and Indian Ocean. The latitude range is 70ºS–70ºN (to avoid the main sea ice covered areas), considering the Southern Ocean sectors of each basin a part of the respective oceans.

Fig. 25 shows annual and seasonal (DJF and JJA) cross sections of the zonally averaged (for each degree of latitude) PC20 and FC21 $H_S$ for the three ocean basins (including their respective Southern Ocean sections). An expected increase in wave heights in the mid-to-high latitudes of the Southern Hemisphere is visible in all cases, especially during JJA (austral winter) in the Indian and Atlantic sectors, reaching ~50 cm and ~30 cm respectively (Fig. 25c,i). Projected decreases are observable mostly in the North Atlantic Ocean (as seen in Figs. 9c, 10c and 11c), but also in the North Pacific Ocean (Figs. 25d,e,f) and between 0º–30ºS in the Indian Ocean in DJF (Fig. 25h), however, these differences are less intense, and do not exceed 25 cm. In the tropical and low latitudes the $H_S$ mean differences are also very small.

In the high latitudes, the previously mentioned projected sea ice cover retraction and the creation of ice free zones can have an impact in the latitudinal position of the projected climatological maximum values of $H_S$ (and $P_w$), shifting them to higher latitudes, in line with the poleward shift of the extratropical storm tracks (Bengtsson *et al.*, 2006). This poleward shift is only noticeable in some sectors of the Southern Ocean, though (Figs. 25b,e,i, for instance). In most cases it does not suffer any considerable alteration. Nevertheless, wave heights are expected to increase in these locations, and new areas of open sea are easily noticeable along the FC21 line, near its top limit (70ºN/S).
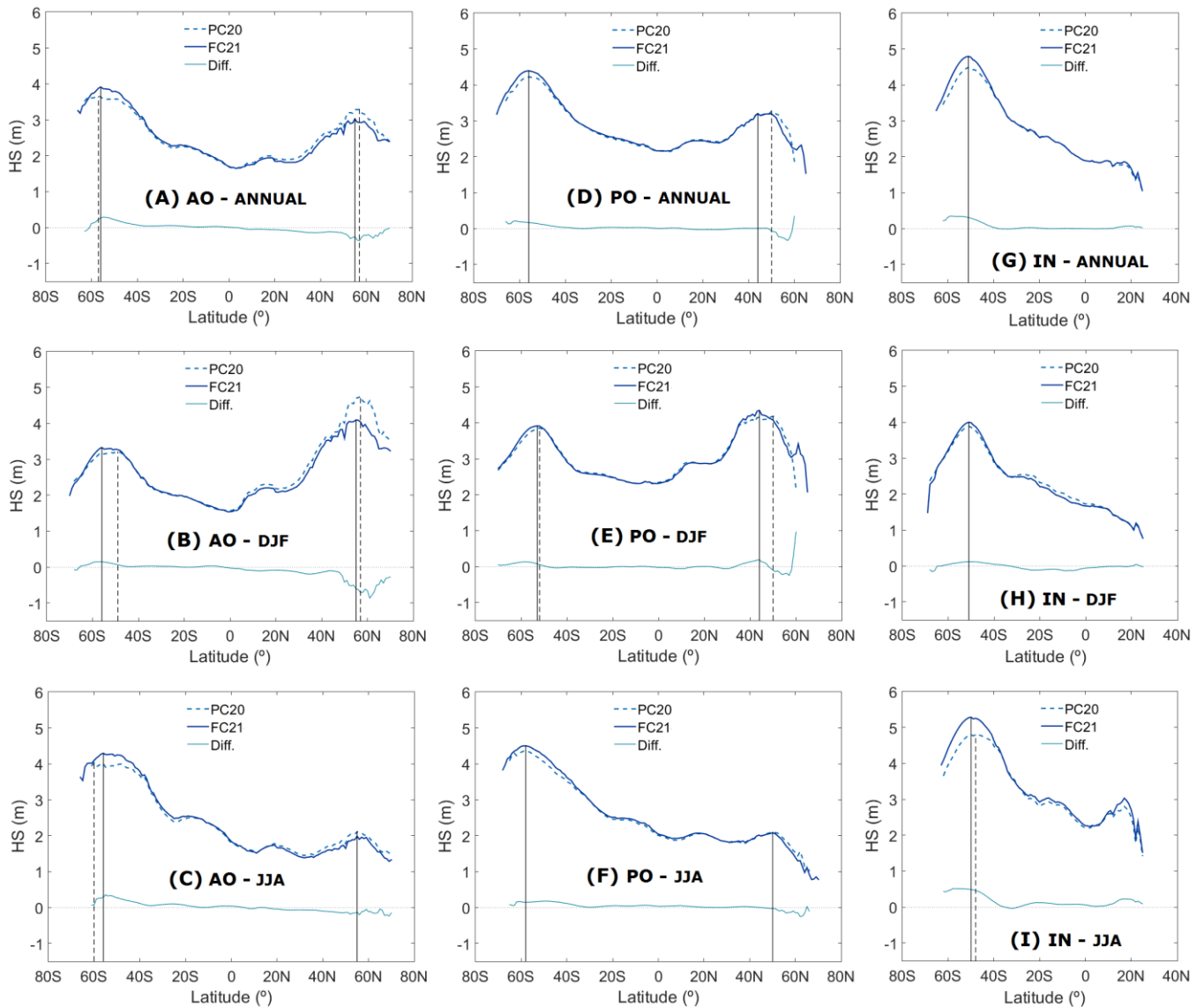


*Figure 25 - Meridional cross sections of the zonally total mean annual, DJF and JJA $H_S$ for PC20 (dashed line) and FC21 (full line) over three individual basins: annual values in the (A) Atlantic Ocean, (D) Pacific Ocean and (G) Indian Ocean, DJF values in the (B) Atlantic Ocean, (E) Pacific Ocean and (H) Indian Ocean, and JJA values in the (C) Atlantic Ocean, (F) Pacific Ocean and (I) Indian Ocean. The light blue line shows the difference between FC21 and PC20 means. The vertical full and dashed black lines represent the latitudes of FC21 and PC20 maximum climatological values, for each Hemisphere.*

The annual and seasonal (DJF and JJA) cross sections of the zonally averaged (for each degree of latitude) PC20 and projected FC21 $P_w$ along the three major ocean basins can be found in Fig. 26. Like in the previous figure, projected increases in wave energy fluxes are visible along the three sectors of the Southern Ocean, especially in the Indian and Atlantic in the austral winter (JJA; Figs. 26c,i), where the differences between the zonal mean values (FC21 minus PC20) surpass the 40 W/m and the 20 W/m, respectively. In the North Atlantic Ocean, on the other hand, slight decreases in the mean zonal wave power can be expected from the Equator, with magnitude increasing with latitude, until they reach 50 W/m around 55ºN in DJF (Fig. 26b). Poleward shifts in the projected $P_w$ climatological maximum values are only visible in Figs. 26b,e,i. The majority of the latitudinal differences are close to zero, and equatorward shifts are visible in Figs. 26a,b,c,d,e.
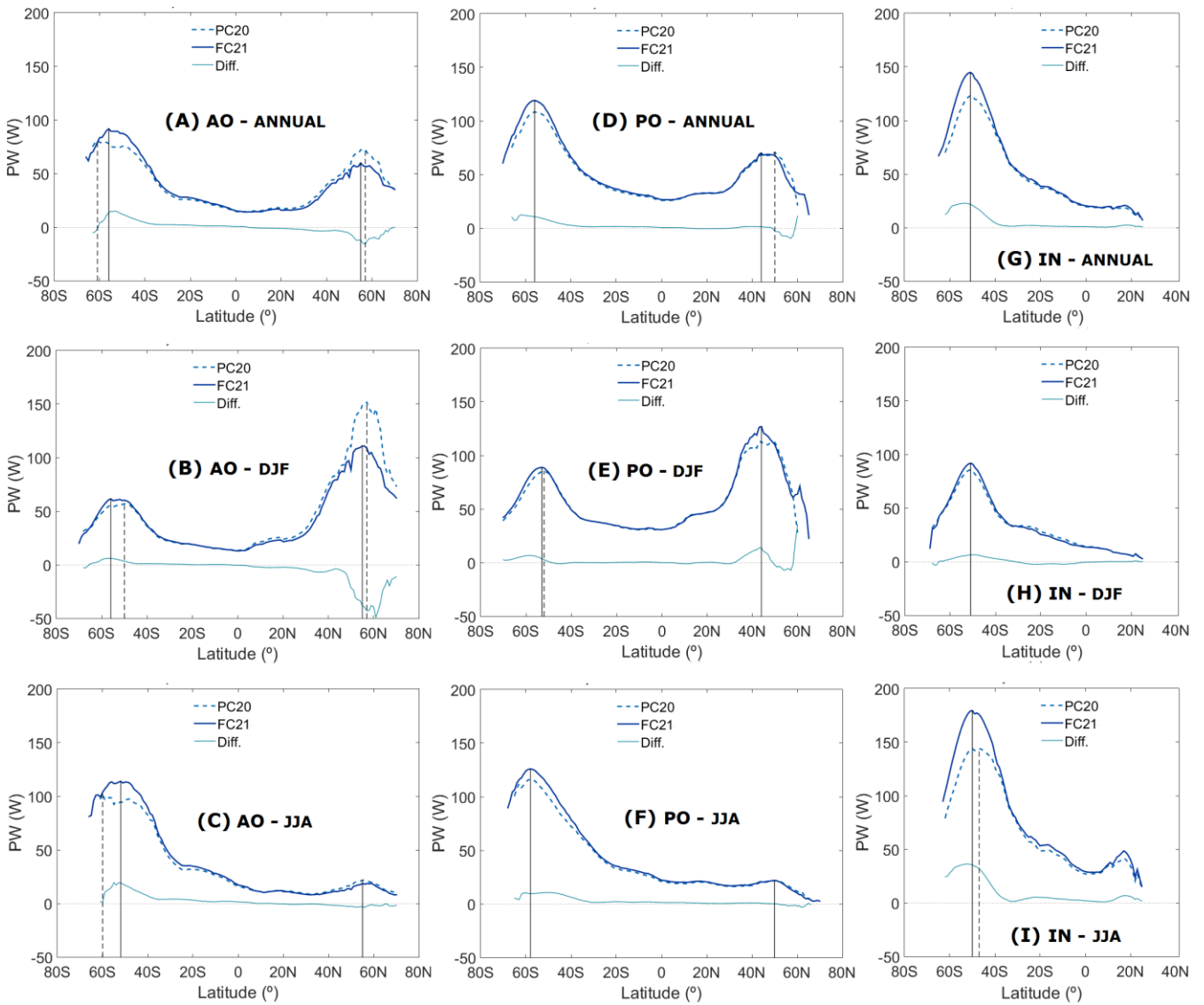


*Figure 26 – As in Fig. 25, but for Pw.*

In the two previous figures and in sections 4 and 5, a direct comparison between the PC20 and FC21 time-slices (1971-2000 compared to 2071-2100) was presented. Nevertheless, it is also valuable to investigate what changes are projected to occur along the whole twenty-first century (from 2006 to 2100), and not just by the end of it. Observations and model reanalyzes suggest that wave heights had been increasing since the 1970s until the end of the twentieth century, in the Northern (WASA Group, 1998; Gulev and Hasse, 1999; Wang and Swail, 2001; Gulev and Grigorieva, 2006; Bromirski *et al.*, 2005) and Southern (Hemer *et al.*, 2010) hemispheres. This global increase in $H_S$ was linked to an increase in the global $U_{10}$ (Sterl and Caires, 2005), but, as mentioned in the beginning of this study, the connection between these two variables is not necessarily direct due to the propagating effect of waves (in the form of swell), and the increases found for $H_S$ may not be straightly linked to the local $U_{10}$ variability. Recent studies have shown that since the beginning of the twenty-first century global wave heights trends have more or less stagnated (Young and Babanin, 2011), with no clear statistically significant trend for mean monthly values.

Fig. 27 shows the annual, DJF and JJA global mean patterns of the two ensemble members linear trends for $H_S$ and $P_w$ until the end of the twenty-first century, covering the period from 2006 to 2100 (FC21F henceforth). These results were obtained by applying a linear trend to each gridpoint of their annual and seasonal means, yearly, for the entire time-slice.
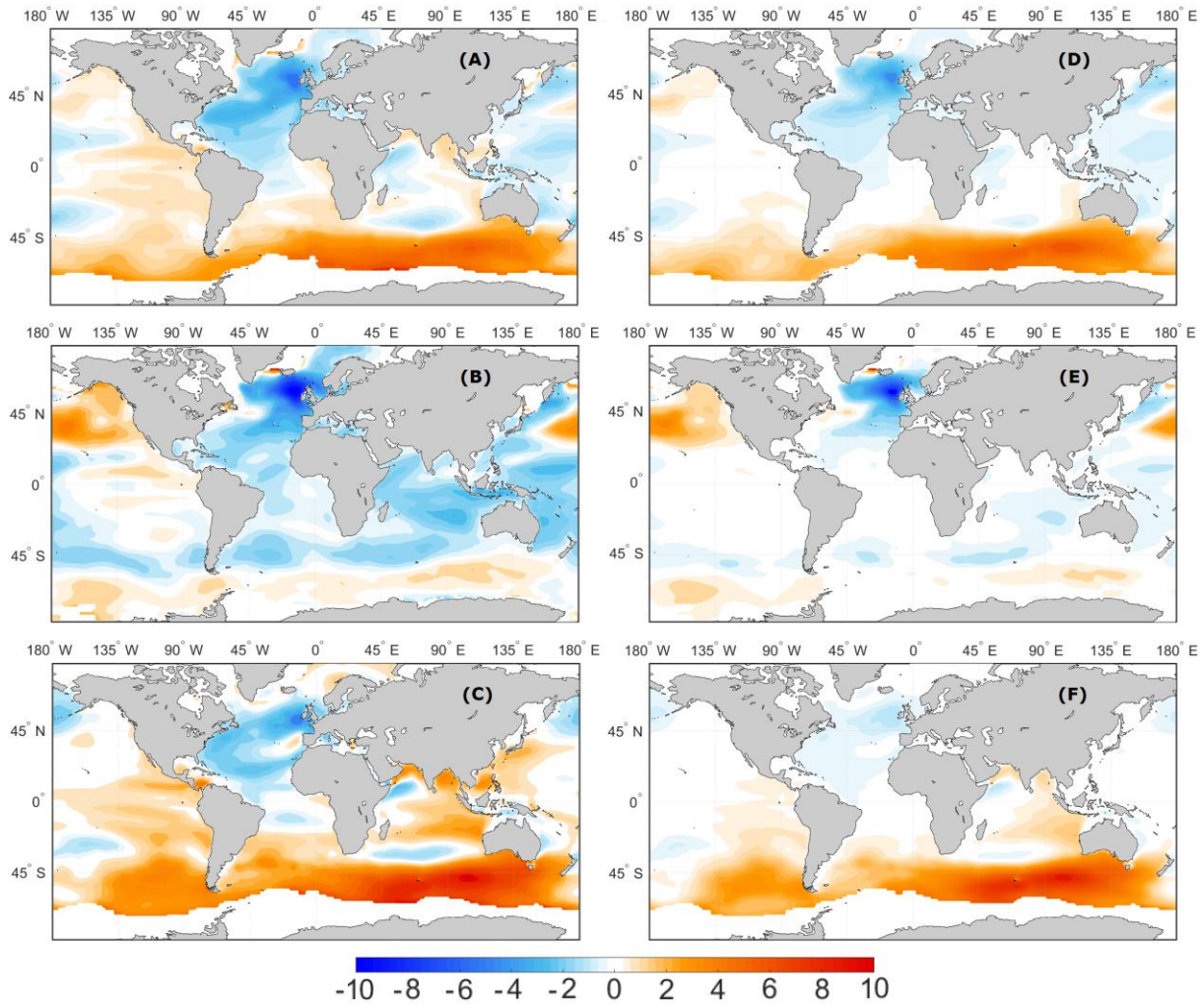
*Figure 27 – FC21F linear trends of Hs (cm/decade) (A) annual, (B) DJF and (C) JJA and Pw (W/m/decade) (D) annual, (E) DJF and (F) JJA.*

The largest projected upward annual changes in both fields (Figs. 27a,d) take place in the Atlantic and Indian sectors of the Southern Ocean, reaching 8 cm/decade and 6 W/m/decade, respectively. Slightly less intense, but wide positive annual $H_S$ tendencies can be expected in the Eastern Pacific Ocean (2 cm/decade) and in the Northeastern Indian Ocean (1-2 cm/decade). Projections show a mean global wave height growth tendency of +0.41 cm/decade. Wave power projected trends are more spatially restricted to the extratropical regions, since near-zero values are present along the low latitudes. The simulations show a mean global growth rate of +0.36 W/m/decade. Considerably steady decreases in $H_S$ and $P_w$ can be expected for the North Atlantic Ocean (in line with the previous results), especially West of the British Isles (-4 to -6 cm/decade; -4 to -5 W/m/decade; Figs. 27a,d), peaking during DJF, the local winter (-8 to -10 cm/decade; -8 to -9 W/m/decade). Throughout DJF (Figs. 27b,e), downward changes in wave height are also expected for the South Atlantic

Ocean (as far as -3 cm/decade), the Western Pacific Ocean (-2 to -4 cm/decade) and the Indian Ocean (-1 to -4 cm/decade). The highest projected positive trends for this period are located in the extratropical latitudes of the North Pacific Ocean, reaching 5 cm/decade and 5 W/m/decade for both $H_S$ and $P_w$. Nevertheless, projections exhibit a mean global negative tendency: -0.39 cm/decade and -0.04 W/m/decade, respectively.

During JJA, the Southern Ocean dominates the projected tendencies, with the highest upward movements in wave height, that will directly affect the respective energy flux field. From Figs. 27c,f, $P_w$ increments of 8-10 cm/decade and 6-8 W/m/decade can be expected, southwest of Australia. Positive trends expand to the Indian and South Pacific Oceans, reaching 4 cm/decade and 1 W/m/decade near the Equator. For these reasons the global mean projected trends for the austral winter are of +0.98 cm/decade and +0.66 W/m/decade, for $H_S$ and $P_w$, respectively.

# 7.    Summary and conclusions

Projected changes in the major wave fields ($H_S$, $U_{10}$, $T_m$, MWD and $P_w$) towards the end of the twenty-first century were analyzed from a dynamical wave global simulation, produced with dynamical wave model WAM, composed by a two member "coherent" ensemble, driven by present-day and potential future atmospheric conditions from EC-Earth, under the RCP8.5 high emissions scenario. The main conclusions of this study are presented in this section.

Firstly, the present climate (PC20-1,4) $H_S$, $T_m$ and $P_w$ fields were compared to the ERA-Interim reanalysis, and buoy observations. The results of these comparisons and validation of the present climate ensemble members were shown in Figs. 2-8. The agreement between the PC20-1,4, the reanalysis, and the buoy observations (better than in Semedo *et al.*, 2013 and in Hemer *et al.*, 2013a) showed that WAM is able produce realistic scenarios of the global wave climate at the end of the twentieth century, providing the necessary confidence in the wave model (WAM) to reproduce the global wave climate by the end of the twenty-first century.

Due to global climate warming, the annual mean values of $H_S$ were shown to be projected to have statistically significantly increases, mainly in the Southern Ocean, by the end of the twenty-first century (Fig. 9c), which is related to the projected intensification of the westerlies ($U_{10}$) there (Fig. 12). Wave height increases in the subtropical latitudes of the Southeastern Pacific Ocean were also shown to be expected for the end of the twenty-first century. These patterns are expected to be maximized during JJA (austral winter), including in the tropical and subtropical regions of the Indian Ocean (Fig. 11c). Statistically significant annual decreases were shown to be projected to occur mainly in the North Atlantic Ocean, but also in the Western Pacific Ocean (Fig. 9c), these being more intense during DJF (Fig. 10c). Due to the expected sea ice cover retraction in the future climate, increases in wave height are visible in the high latitudes at an annual (Fig. 9c) and seasonal scales (Figs. 10c and 11c). The summarized global mean $H_S$ normalized differences (future projected climate minus present climate normalized by present climate; annual, DJF and JJA) are presented in Table 2, for each ensemble member in particular, and for their ensemble mean.

*Table 2 – Global mean values (%) for each ensemble member (and the mean of both) normalized differences of Hs between future (projected) and present climates (FC21 minus PC20 normalized by PC20).*

| Member (H$_S$; %) | Annual | DJF | JJA |
|---|---|---|---|
| FC21-1 | +0.89 | -0.88 | +2.77 |
| FC21-4 | +1.28 | -0.49 | +2.51 |
| MEAN (1,4) | **+1.07** | **-0.69** | **+2.60** |

The mean annual and seasonal (DJF and JJA) portions of the global ocean in which increases in H$_S$ were shown to be projected to occur (areas with positive normalized differences divided by the global ocean area) are summarized in Table 3. During JJA, when the mean global wave height projected increases presented a higher value (+ 2.60%), almost three quarters of the global ocean can expect an increase in H$_S$ (73.93%). This portion is higher for the ensemble member nr. 1 singularly, reaching 77.84%.

*Table 3 – Portion of the global ocean area that detains a Hs positive normalized differences covering, for each ensemble member, and for the mean of both.*

| Member (H$_S$; %) | Annual | DJF | JJA |
|---|---|---|---|
| FC21-1 | 61.98 | 51.30 | 77.84 |
| FC21-4 | 66.77 | 55.86 | 68.20 |
| MEAN (1,4) | **64.82** | **53.42** | **73.93** |

T$_m$ mean annual and seasonal values were shown to be projected to increase almost everywhere but the North Atlantic and West Pacific oceans, in DJF. The reason for these results lay on two factors: the fact that projected increases in H$_S$, specifically in the Southern Ocean, lead to higher wave heights (and wave energy) at the generation areas, and the fact that the retraction of the sea ice cover extent in the high latitudes (also more relevant in the Southern Hemisphere) creates additional free space for wave propagation (supported by the MWD analysis (section 4.3) and Figs. 25b,e,i, for instance), enabling waves with longer periods near the Equator, at the "swell pools". In fact, some of the highest statistically significant projected increases in T$_m$ are projected to occur along the low and tropical latitudes. The summarized global mean T$_m$ normalized differences (future projected climate minus present climate normalized by present climate) at an annual and seasonal (DJF and JJA) scales are presented in Table 4, for each ensemble member in particular, and the mean of both.

*Table 4 – Global mean values (%) for each ensemble member (and the mean of both) normalized differences of Tm between future (projected) and present climates (FC21 minus PC20 normalized by PC20).*

| Member ($T_m$; %) | Annual | DJF | JJA |
|---|---|---|---|
| FC21-1 | +1.32 | +0.44 | +2.25 |
| FC21-4 | +1.45 | +0.61 | +1.95 |
| MEAN (1,4) | **+1.39** | **+0.52** | **+2.09** |

The mean annual and seasonal (DJF and JJA) portions of the global ocean in which increases in $T_m$ were shown to be projected to occur (areas with positive normalized differences divided by the global ocean area) are summarized in Table 5. Similarly to the $H_S$ results, it is during JJA that the largest portion of the global ocean shows $T_m$ positive normalized differences covering, of 87.48% for the mean of both ensemble members, but reaching 90.08% when taking member nr. 1 singularly.

*Table 5 – Portion of the global ocean area that detens a Tm positive normalized differences covering, for each ensemble member, and for the mean of both.*

| Member ($T_m$; %) | Annual | DJF | JJA |
|---|---|---|---|
| FC21-1 | 78.75 | 67.30 | 90.08 |
| FC21-4 | 80.74 | 72.42 | 85.13 |
| MEAN (1,4) | **79.99** | **71.14** | **87.48** |

Projected changes in the future mean wave direction field were addressed in Figs. 16, 17 and 18. Wave front direction plays an important role in shoreline risk analysis, for instance, since directional change in the mean wave front can lead to intensification (or decreases) of local erosion events. The annual anomalies (FC21 minus PC20) displayed in Fig. 16c showed a prevalence of anticlockwise (negative) anomalies along the mid-to-high latitudes of both hemispheres, associated to the shifting of the storm tracks to higher latitudes (Arblaster *et al.*, 2011), and mainly clockwise (positive) anomalies along the tropical and subtropical regions of both hemispheres, consistent with a larger contribution of Southern Ocean swell (Hemer *et al.*, 2013a). Seasonally, negative anomalies were shown to still be present in the extratropical latitudes, but clockwise (positive) anomalies transit mainly to the tropical and subtropical regions of the correspondent summer hemisphere.

Lastly, the analysis of the $P_w$ field towards the end of the twenty-first century showed that the wave power is expected to statistically significantly increase almost in the entire

global ocean except in the North Atlantic and West Pacific during DJF, results that are similar to the $H_S$ ones, since the wave energy flux ($P_w$) is a function of $T_m$ and $H_S$ to the first and second orders, and the changes in $T_m$ fields (on an annual and seasonal scales) tend to be less intense and more homogeneous. Up to 20% projected increases in $P_w$ were found for the Northeastern Pacific Ocean in DJF, and up to 30% along the Indian sector of the Southern Ocean in JJA. The summarized global mean $P_w$ normalized differences (future projected climate minus present climate normalized by present climate) at an annual and seasonal (DJF and JJA) scales are presented in Table 6, for each ensemble member in particular, and the mean of both. The mean global projected FC21 $P_w$ values are, on average, 7.18% higher in the global ocean during JJA, but they remain almost unaltered during DJF, because of the large areas of projected decreases found for this season, that compensate the areas with a contrary projected behavior.

Table 6 – Global mean values (%) for each ensemble member (and the mean of both) normalized differences of Pw between future (projected) and present climates (FC21 minus PC20 normalized by PC20).

| Member ($P_w$; %) | Annual | DJF | JJA |
|---|---|---|---|
| FC21-1 | 3.33 | -0.23 | 7.77 |
| FC21-4 | 4.50 | 0.56 | 6.65 |
| MEAN (1,4) | **3.90** | **0.17** | **7.18** |

The mean annual and seasonal (DJF and JJA) portions of the global ocean in which increases in $P_w$ were shown to be projected to occur (areas with positive normalized differences divided by the global ocean area) are summarized in Table 7. Once again, it is during the austral winter (JJA), that the mean global area covered by projected increases in wave energy flux presented a higher value (81.43%), reaching 83.50% for member nr. 1, and "merely" 75.88% for member nr. 4.

Table 7 – Portion of the global ocean area that detains a Pw positive normalized differences covering, for each ensemble member, and for the mean of both.

| Member ($P_w$; %) | Annual | DJF | JJA |
|---|---|---|---|
| FC21-1 | 67.43 | 56.25 | 83.50 |
| FC21-4 | 71.21 | 61.00 | 75.88 |
| MEAN (1,4) | **70.70** | **58.47** | **81.43** |

Altogether, $H_S$, $T_m$ and $P_w$ wave fields were shown to be projected to increase when comparing the 2071-2100 (FC21) with the 1971-2000 (PC20) time slices, especially during

JJA (Austral winter; Tables 2-6), and excepting for the wave height in DJF (Table 2). Results showed that generally, both ensemble members are in accordance with each other, with the largest disparities found for the $P_w$ field (Tables 5,6).

The interannual variability of the wave height and wave energy flux was investigated by means of an EOF analysis, for the North Atlantic sub-basin. The anomaly patterns found for both variables showed that they are linked to the wind field, being dominated by the higher values present along the extratropical storm belt. On an annual scale, due to climate change, the main centers of action for $H_S$ and $P_w$ were shown to be projected to get weaker (in line with the negative normalized differences found for these fields; Figs. 9c and 19c). Similar behavior was detected for $H_S$ in DJF and JJA. The $P_w$ field, on the other hand, was shown to be expected to get slightly stronger during DJF and JJA, when a ~2° positive latitudinal shifting was also observed in both seasons. Despite this slight poleward shift of the wave power center of action, no shifting of its seasonal (or annual) mean climatological maxima was observed in the Northern Hemisphere (Fig. 26). Shifts of this kind (for $P_w$ but also for $H_S$, in Fig. 25) were only visible in the Southern Hemisphere (along the Southern Ocean), mainly in DJF (austral summer), when the sea ice cover retraction process is maximized (Figs. 25b,e,i and Figs. 26b,e,i, for instance).

Finally, the 2006-2100 $H_S$ and $P_w$ global mean (of the two ensemble members) linear trends were presented, in which, once again, the major projected increases in both fields were visible for the Southern Ocean, reaching 8-10 cm/decade and 6-8 W/m/decade, respectively, southwest of Australia (Figs. 27c,f). Relevant projected decreases were also shown to be present for the North Atlantic Ocean (between -8 to -10 units of wave height and power per decade; Figs. 27b,e). Along the tropical and subtropical latitudes, lower tendencies were generally found, especially for $P_w$ (ranging from -2 to 2 W/m/decade).

The summarized global mean $H_S$ projected linear trends for the 2006-2100 time-slice, at an annual and seasonal (DJF and JJA) scales are presented in Table 8, for each ensemble member in particular, and the mean of both. In Table 9, the mean annual and seasonal portions of the global ocean in which positive $H_S$ linear trends were shown to be projected to occur (areas with positive linear trends divided by the global ocean area) are summarized. A global mean annual $H_S$ positive growth rate is visible, of 0.41 cm/decade, peaking during JJA, with 0.982 cm/decade. 74.3% of the global ocean is projected to increase its wave heights in this season. A global negative mean growth rate (of -0.39 cm/decade) is projected to occur

during DJF, clearly connected with the large areas of projected $H_S$ decreases previously shown for the FC21 (2071-2100) time-slice. Also during this season, mean positive $H_S$ trends are only to be expected in 36.18% of the global ocean area, and less for the ensemble member nr. 4 (27.05%).

*Table 8 – Global mean values (cm/decade) for each ensemble member (and the mean of both) Hs linear decadal trends.*

| Member ($H_S$; cm/d) | Annual | DJF | JJA |
|---|---|---|---|
| FC21F-1 | 0.34 | -0.31 | 0.88 |
| FC21F-4 | 0.47 | -0.44 | 1.06 |
| MEAN (1,4) | **0.41** | **-0.39** | **0.98** |

*Table 9 – Portion of the global ocean area that detains a Hs positive linear decadal trend covering, for each ensemble member, and for the mean of both.*

| Member ($H_S$; %) | Annual | DJF | JJA |
|---|---|---|---|
| FC21F-1 | 60.34 | 42.48 | 74.37 |
| FC21F-4 | 61.95 | 27.05 | 71.61 |
| MEAN (1,4) | **62.40** | **36.18** | **74.32** |

The summarized global mean $P_w$ projected linear trends for the 2006-2100 time-slice, at an annual and seasonal (DJF and JJA) scales are presented in Table 10. The mean annual and seasonal portions of the global ocean in which positive $P_w$ linear trends were shown to be projected to occur (areas with positive linear trends divided by the global ocean area) are summarized in Table 11. Both Table 10 and Table 11 exhibit results for each ensemble member in particular, and the mean of both. $P_w$ growth rates show a similar behavior to the $H_S$ ones, but less extreme values: the global mean annual wave power projected tendency is set on 0.36 W/m/decade, peaking during JJA, with 0.66 W/m/decade, being positive in 80.98% of the global ocean area in this period. In the boreal winter (DJF), the mean global $P_w$ field can expect a slight decrease, of -0.04 W/m/decade.

*Table 10 – Global mean values (cm/decade) for each ensemble member (and the mean of both) Pw linear decadal trends.*

| Member ($P_w$; W/m/d) | Annual | DJF | JJA |
|---|---|---|---|
| FC21F-1 | 0.33 | -0.0004 | 0.62 |
| FC21F-4 | 0.38 | -0.08 | 0.68 |
| MEAN (1,4) | **0.36** | **-0.04** | **0.66** |

Table 11 – *Portion of the global ocean area that detains a Pw positive linear decadal trend covering, for each ensemble member, and for the mean of both.*

| Member ($P_w$; %) | Annual | DJF | JJA |
|---|---|---|---|
| FC21F-1 | 68.76 | 46.63 | 80.00 |
| FC21F-4 | 66.93 | 30.49 | 78.20 |
| MEAN (1,4) | **68.61** | **43.20** | **80.98** |

In this thesis the fundamental features of projected changes in the $H_S$, $U_{10}$, $T_m$, MWD and $P_w$ wave fields climates for the end of the twenty-first were presented, based on, from a 2-member single scenario (RCP8.5) "coherent" ensemble of GLOWAVES-2 simulations. These parameters are able to characterize a wave field with a certain degree of detail, although, there are still some limitations, mainly concerning the inner properties of the sea state: for instance, two fields with the same significant wave height and period (and consequently the same energy flux) can still be very different in detail, since different portions of wind sea and swell waves can generate identical values for these parameters alone. The use of a single GCM forcing and a single emission scenario poses another limitation to the results of this study, although, they are in line with results of previous studies (Mori *et al.*, 2010; Semedo *et al.*, 2013; Hemer *et al.*, 2013a; Dobrynin *et al.*, 2012, for instance). A larger ensemble of global wave climate simulations, using atmospheric forcing from different climate models and a larger range of emission scenarios is needed to fully assess the robustness of the features shown in this study. A major global wave climate ensemble is one of the main COWCLIP project objectives.

# References

Alves, J. H. G. M. (2006). Numerical modeling of ocean swell contributions to the global wind wave climate. *Ocean Modelling*, 11 (1-2), 98-122.

Arblaster, J. M., Meehl, G., Karoly, D. J. (2011). Future climate change in the Southern Hemisphere: Competing effects of ozone and greenhouse gases. *Geophysical Research Letters*, 38, 1-6, DOI: 10.1029/2010GLo45384.

Ardhuin, F., Chapron, B., Collard, F. (2009). Observation of swell dissipation across oceans. *Geophysical Research Letters*, 36(6): L06607.

Barber, N. F., Ursell, F. (1948). The generation and propagation of ocean waves and swell. I. Wave periods and velocities. *Philosophical Transactions*, Royal Society of London, 240A, 527-560.

Bengtsson, L., Hodges, K., Roeckner, E. (2006). Storm tracks and climate change. *Journal of Climate*, 19, 3518-3543.

Bidlot, J.-R., Janssen, P., Abdalla, S. (2007). A revised formulation of the ocean wave dissipation and its model impact. *ECMWF Technological Memo.*, 509.

Björnsson, H., Venegas, S. A. (1997). A Manual for EOF and SVD analyses of Climatic Data. McGill University.

Bromirski, P. D., Duennebier, F. K., Stephen, R. A. (2005) Mid-ocean microseisms. *Geochemistry, Geophysics, Geosystems*, 6, Q04009, DOI: 10.1029/2004GC000768.

Chen, G., Chapron, B., Exraty, R., Vandemark, D. (2002). A global view of swell and wind sea climate in the ocean by satellite altimeter and scatterometer. *Journal of Atmospherical and Oceanic Technologies*, 19, 1849-1859.

Coelho, C., Silva, R., Veloso-Gomes, F., Taveira-Pinto, F. (2009). Potential effects of climate change on northwest Portuguese coastal zones. ICES, *Journal of Marine Sciences*, 66, 1497-1507.

Dee, D. P., Uppala, S. (2009). Variational bias correction of satellite radiance data in the ERA-Interim reanalysis. *Quarterly Journal of the Royal Meteorological Society*, 135, 1830-1841.

Dee, D. P., and Coauthors. (2011). The ERA-Interim reanalysis: configuration and performance of the data assimilation system. *Quarterly Journal of the Royal Meteorological Society*, 137, 1830-1841.

Dobrynin, M., Murawsky, J., Yang, S. (2012). Evolution of the global wind wave climate in CMIP5 expriments. *Geophysical Research Letters*, 39, DOI:10.1029/2012GL052843.

Dobrynin, M., Murawski, J., Baehr, J., Ilyina, T. (2015). Detection and Attribution of Climate Change Signal in Ocean Wind Waves. *Journal of Climate*, 28, 4, 1578-1591.

Erikson, L. H., Hegermiller, C. A., Barnard, P. L., Ruggiero, P., van Ormondt, M. (2015). Projected wave conditions in Eastern North Pacific under the influence of two CMIP5 climate scenarios. *Ocean Modelling*, 96, 1, 171-185.

Fan, Y., Held, I. M., Lin, S.-J., Wang, X. L. (2013). Ocean warming effect on surface gravity wave climate change for the end of the 21st century. *Journal of Climate*, 26, 6046-6066.

Gulev, S. K., Hasse, L. (1999). Changes in wind waves in the North Atlantic over the last 30 years. *International Journal of Climatology*, 19, 1091-1018.

Gulev, S. K., Grigorieva, V., Sterl, A., Woolf, D. (2003). Assessment of the reliability of wave observations from voluntary observing ships: Insights from the validation of a global wind wave climatology based on voluntary observing ship data. *Journal of Geophysical Research*, 108, 3236, DOI: 10.1029/2002JC001437.

Gulev, S. K., Grigorieva, V. (2006). Variability of the Winter Wind Waves and Swell in the North Atlantic and North Pacific as Revealed by the Voluntary Observing Ship Data. *Journal of Climate*, 19, 5667-5685.

Hazeleger, W., and Coauthors. (2010). EC-Earth: A seamless earth-system prediction approach in action. *Bulletin of the American Meteorological Society*, 91, 1357-1363. DOI: 10.1175/2010BAMS20877.1.

Hemer, M. A., Church, J. A., Hunter, J. R. (2010). Variability and trends in the directional wave climate of the Southern Hemisphere. *International Journal of Climatology*, 30, 475-491.

Hemer, M. A., Wang, X. L., Weisse, R., Swail, V. R., COWCLIP Team. (2012). Advancing wind-waves climate science – The COWCLIP Project. *Bulletin of the American Meteorological Society*, DOI: 10.1175.

Hemer, M., Fan, Y., Mori, N., Semedo, A., Wang, X. (2013a). Projected changes in wave climate from a multi-model ensemble. *Nature Climate Change*, 3, 471-476, DOI: 10.1038/NCLIMATE1791.

Hemer, M. A., Trenham, C. E. (2015). Evaluation of a CMIP5 derived dynamical global wind wave climate model ensemble. *Ocean Modelling*, 103, DOI: 10.1016/j.ocemod.2015.10.009.

Hogben, N., Lumb, F. E. (1967). Ocean Wave Statistics, London: Her Majesty's Stationery Office (HMSO).

Hogben, N., Dacunha, N. M. C., Oliver, G. F., (1986). Global Wave Statistics. London: Unwin Brothers.

IPCC-AR4. (2007). Climate Change 2007: The Physical Science Basis. Cambridge: Cambridge University Press.

IPCC-AR5. (2013). Climate Change 2013: The Physical Science Basis. Cambridge: Cambridge University Press.

Janssen, P. A. E. M. (1991). Quasi linear theory of wind wave generation applied to wav forecasting. *Journal of Physical Ocanography*, 21, 1631-1642.

Janssen, P. A. E. M. (2004). The Interaction of Ocean Waves and Wind. Cambridge: Cambridge University Press.

Kang, S., Lu, J. (2012). Expansion of the Hadley Cell under Global Warming: Winter versus Summer. *American Meteorological Society*, 25, 8387-8393.

Kinsman, B. (1965). Wind waves, their generation and propagation on the ocean surface. Englewood Cliffs, NJ. Prentice-Hall.

Komen, G. J., Cavalieri, L., Doneland, M., Hasselmann, S., Janssen, P. A. E. M. (1994). Dynamics and modeling of ocean waves. Cambridge: Cambridge University Press.

Mei, C. C. (1983). The applied dynamics of ocean surface waves, Wiley.

Miles, R. (1957). On the generation of waves by shear flows. *Journal of Fluid Mechanics*, 3, 185-204.

Mori, N., Yasuda, T., Mase, H., Tom, T., Oku, Y. (2010). Projections of extreme wave climate change under global warming. *Hydrological Research Letters*, 4, 15-19.

Munk, W. H. (1944). Proposed uniform procedure for observing waves and interpreting instrument records. California: Wave Project at the Scripps Institute of Oceanography.

Munk, W. H. (1951). Origin and generation of waves. *Proc. First Coastal Engineering Conference*, Long Beach, California, 1-4.

Munk, W. H., Miller, G. R., Snodgras, F. E., Barber, N. F. (1963). Directional recording of swell from distant storms. *Philosophical Transactions*, Royal Society of London, 255, 505-584.

Phillips, O. M. (1957). On the generation of waves by a turbulent wind. *Journal of Fluid Mechanics*, 2, 417-445.

Semedo, A., Sušelj, K., Rutgersson, A., Sterl, A. (2011). A Global View on the Wind Sea and Swell Climate and Variability from EERA-40. *Journal of Climate*, 24, 5, 1461-1479.

Semedo, A., Behrens, R., Sterl, A., Bengtsson, L., Günther, H. (2013). Projection of Global Wave Climate Change toward the End of the Twenty-First Century. *Journal of Climate*, 26, 8269-8288.

Semedo, A., Vettor, R., Breivik, Ø., Sterl, A., Reistad, M., Soares, C. G., Lima, D. (2014). The wind sea and swell waves climate in the Nordic seas. Ocean Dynamics, DOI: 10.1007/s10236-014-0788-4.

Semedo, A., Soares, P. M. M., Lima, D. C. A., Cardoso, R. M., Bernardino, M., Miranda, P. M. A. (2015). The impact of climate change on the global coastal low-level wind jets: EC-EARTH simulations. *Global and Planetary Change*, 137, 88-106.

Snodgrass F. E., Groves, G. W., Haselmann, K., Miller, G. R., Munk, W. H., Powers, W. H. (1966). Propagation of ocean swell across the Pacific. *Philosophical Transactions*, Royal Society of London, A249, 431-497.

Solomon, S., Qin, D., Manning, M., Chen, Z., Marquis, M., Averyt, K. B., Tignor, M., Miller Jr, H. L. (2007). Climate Change 2007: The Physical Science Basis. *Cambridge University Press*, 996.

Sterl, A. (2004). On the (in)Homogeneity of Reanalysis Products. *Journal of Climate*, 17, 3866-3873.

Sterl, A., Caires, S. (2005). Climatology, variability and extrema of ocean waves: The web-based KNMI/ERA-40 wave atlas. *International Journal of Climatology*, 25, 963-977.

Tuomi, L., Kahma, K., Pettersson, H. (2011). Wave hindcast statistics in the seasonally ice-covered Baltic Sea. *Boreal Environment Research*, 16, 451-472.

Uppala, S. M. (1997). Observing system performance in ERA, ECMWF Re-Analysis Project Report Series 3, ECMWF.

Uppala, S. M., and Coauthors. (2005). The ERA-40 reanalysis. *Quarterly Journal of the Royal Meteorological Society*, 131, 2961-3012.

von Storch, H., Zwiers, F. (1999). Statistical Analysis in Climate Research. Cambridge: Cambridge University Press.

WAMDI Group. (1988). The WAM Model – A Third Generation Ocean Wave Prediction Model. *Journal of Physical Oceanography*, 18, 1775-1810.

Wang, X. L., Swail, V. R. (2001). Changes of Extreme Wave Heights in Northern Hemisphere Oceans and Related Atmospheric Circulation Regimes. *Journal of Climate*, 14, 2204-2221.

Wang, X. L., Feng, Y., Swail, V. R. (2015). Climate change signal and uncertainty in CMIP5-based projections of global ocean surface wave heights. *Journal of Geophysical Research*, 120, 5, 3859-3871.

WASA Group. (1998). Changing waves and storms in the northeast Atlantic? *Bulletin of the American Meteorological Society*, 79, 741-760.

Young, I. R. (1999). Seasonal variability of the global ocean wind and wave climate. *International Journal of Climatology*, 19, 931-950.

Young, I. R., Zieger, S., Babanin, V. (2011). Global trends in wind speed and wave height. *Science*, 332, 451-455.